Advances in Aircraft and Spacecraft Science, *Vol. 2, No. 2 (2015) 125-168*
DOI: http://dx.doi.org/10.12989/aas.2015.2.2.125

Phenomenology of nonlinear aeroelastic responses of highly deformable joined wings

Rauno Cavallaro[1,3a], Andrea Iannelli[2b], Luciano Demasi[*1] and Alan M. Razón[1c]

[1]*Department of Aerospace Engineering, San Diego State University, 5500 Campanile Dr., San Diego, CA, USA*
[2]*Department of Aerospace Engineering, University of Pisa, via G.Caruso 8, Pisa, Italy*
[3]*Department of Structural Engineering, University of California San Diego, 9500 Gilman Dr., La Jolla, CA, USA*

(Received July 15, 2014, Revised August 1, 2014, Accepted September 22, 2014)

Abstract. Dynamic aeroelastic behavior of structurally nonlinear Joined Wings is presented. Three configurations, two characterized by a different location of the joint and one presenting a direct connection between the two wings (SensorCraft-like layout) are investigated.

The snap-divergence is studied from a dynamic perspective in order to assess the real response of the configuration. The investigations also focus on the flutter occurrence (critical state) and postcritical phenomena. Limit Cycle Oscillations (LCOs) are observed, possibly followed by a loss of periodicity of the solution as speed is further increased. In some cases, it is also possible to ascertain the presence of period doubling (flip-) bifurcations.

Differences between flutter (Hopf's bifurcation) speed evaluated with linear and nonlinear analyses are discussed in depth in order to understand if a linear (and thus computationally less intense) representation provides an acceptable estimate of the instability properties.

Both frequency- and time-domain approaches are compared. Moreover, aerodynamic solvers based on the potential flow are critically examined. In particular, it is assessed in what measure more sophisticated aerodynamic and interface models impact the aeroelastic predictions.

When the use of the tools gives different results, a physical interpretation of the leading mechanism generating the mismatch is provided. In particular, for PrandtlPlane-like configurations the aeroelastic response is very sensitive to the wake's shape. As a consequence, it is suggested that a more sophisticate modeling of the wake positively impacts the reliability of aerodynamic and aeroelastic analysis.

For SensorCraft-like configurations some LCOs are characterized by a non-synchronous motion of the inner and outer portion of the lower wing: the wing's tip exhibits a small oscillation during the descending or ascending phase, whereas the mid-span station describes a sinusoidal-like trajectory in the time-domain.

Keywords: joined wings; limit cycle oscillations; aeroelasticity; flutter; bifurcations

1. Introduction

∗Corresponding author, Associate Professor, E-mail: ldemasi@mail.sdsu.edu
[a]Ph.D. Candidate, E-mail: rauno.cavallaro@gmail.com
[b]Visiting Graduate Student, E-mail: andrea.iannelli.uni@gmail.com
[c]Undergraduate Student, E-mail: ae.alan.marquez@gmail.com

http://www.techno-press.org/?journal=aas&subpage=7 ISSN: 2287-528X (Print), 2287-5271 (Online)

There is currently great interest in innovative aircraft configurations. Among them, joined-wing concept (Wolkovitch 1986, Frediani *et al. 2012*) has captured the attention as a possible candidate for the airplane of the future. However, it was argued and also demonstrated that a reasonably accurate conceptual/preliminary design is hard to be pursued due to inherent structural nonlinearities that may invalidate the results obtained with fast lower fidelity tools, which are a necessity when exploring the large parameters' space typical of the early design stages. For example, references (Blair *et al.* 2005, Demasi *et al.* 2013a, Cavallaro *et al.* 2012, Cavallaro *et al.* 2014a) showed non-negligible differences when comparing structural responses obtained with linear and nonlinear capabilities.

Further difficulties arise from the inherently overconstrained nature of this layout. As a consequence, consolidated design strategies and tools developed in decades, and effectively used by the industry, have to be reviewed. This represents one of the major barriers to the development of Joined Wings (Chambers 2005).

The necessity of including structural nonlinearities early in the design has pushed researchers (Demasi and Livne 2007, Demasi and Palacios 2010) to try to achieve computational efficiency with reduced order models. However, results in this direction have not been quite encouraging. Some recent efforts are shown in (Tiso *et al.* 2014, Phlipot *et al.* 2014).

The situation outlined in (Cavallaro *et al.* 2013b) goes well beyond a bad prediction of the critical condition. It is in fact shown that bi-stability is possible and thus, catastrophic branch-jumping may eventually arise well before the static limit condition is reached. The only tool to detect such regions is a nonlinear full postcritical analysis (branch tracking). Actually, this may not be enough to plot the complete static equilibrium diagram: *isola*-type bifurcations are shown.

When assessing joined-wing behavior from a static aeroelastic perspective, similar problems were noticed (Demasi *et al.* 2013b) in terms of presence of bi-stable regions, and the snap-divergence concept was introduced. The strong structural nonlinearities have demonstrated to be dominant also for small angles of attack and attached flow.

However, a complete scenario of the aeroelastic properties may be sketched only by nonlinear dynamic investigations. To the best of authors' knowledge, nonlinear aeroelastic dynamic analysis was pursued only in a few efforts, i.e., references (Demasi and Livne 2009a, Bhasin *et al.* 2012). The first of these preliminary studies showed how flutter speed prediction varied when structural nonlinearities were included in the model, whereas the second study presented a gust-induced limit cycle oscillation.

The effort of this paper is in the direction of showing, studying and gaining insight into the dynamic aeroelastic phenomena inherent to these configurations, which have potential impact on the design of Joined Wings.

2. Contributions of the present study

Past numerical investigations presented in references (Demasi *et al.* 2013a, Cavallaro *et al.* 2012, Cavallaro *et al.* 2013a, Demasi *et al.* 2013b, Cavallaro *et al.* 2014a) characterized the response of Joined Wings on a conceptual level. In particular, a snap-instability was first found (Demasi *et al.* 2013a) when statically loading the structure with mechanical forces. The occurrence of such kind of instability (saddle-node bifurcation, refer to Seydel 2009 for more details) was also observed when mechanical forces of a follower type (Cavallaro *et al.* 2013a) or aerodynamic loads

(Demasi *et al.* 2013b) were considered. For the true aeroelastic case, the static instability was named *snap-divergence*, in order to resemble the snap-phenomenon that was arising in the pure mechanical case, even if a real snap may practically not occur due to the nonconservative nature of aerodynamic forces. One of the contributions of this paper is the study of this phenomenon from a dynamic point of view: after assessing, by means of a series of linearized frequency-domain analyses, that the flutter speed is higher than the snap-divergence one, the true dynamic response will be shown.

In reference (Demasi *et al.* 2013b) the *snap-divergence* was compared to the traditional divergence analysis, performed through an eigenvalue analysis about particular configurations (usually the undeformed one). Discrepancy between the critical speeds predicted by these two approaches was substantial. Moreover, the traditional eigenvalue approach was overpredicting the divergence speed. It is then expected a mismatch between flutter speeds evaluated by means of linear and nonlinear flutter analyses. This will be shown to be important and to have a similar trend as the one found for the divergence analysis: linear tools overpredict the flutter speed, at least for the considered configurations. The above comparison is further augmented by considering different damping ratios and time-domain analyses.

Assessment of flutter speed gives a local information about loss of stability (Hopf's bifurcation), however, does not provide a picture of what happens in the postcritical region (see the works cited in (Dowell *et al.* 2003) for a comprehensive literature review). With the aid of different time-domain capabilities LCOs are shown. For the SensorCraft-like case, it is found an asynchronous motion between the outer and inner part of the lower wing: while the inner part moves in a wave-like pattern, the outer part has a small localized oscillation during the ascending or descending portion of the periodic motion.

A peculiarity of some joined-wing configurations is that, for higher speed, further bifurcation phenomena as *period doubling* (Seydel 2009, Dowell *et al.* 2003, Thompson and Stewart 1986, Strogatz 1994) occur. Moreover, loss of periodicity can also be observed when speed is further increased, suggesting that a transition to chaos may be in place. On the other hand, for other joined-wing layouts experiencing an LCO, increasing the speed may have the opposite effect, leading to a stable steady state.

Previous studies on delta wings showed that when the geometrical structural nonlinearities are important they may also drive the limit cycle oscillation much more than the aerodynamic effects do. References (Gordnier and Melville 2001, Gordnier 2003, Attar and Gordnier 2006) are good examples. Considering the strong structural nonlinearities typical of Joined Wings, it is then natural to investigate under which conditions they play an important role in the development of limit cycle oscillation, which may appear even for a completely attached flow and potential aerodynamics.

An often overlooked issue is the level of confidence that should be expected from the employed solvers. In fact, even within the above mentioned assumptions, there are different levels of approximations. In this paper effects of load/displacements transferring methods (splining, Harder and Desmarais 1972, meshless, Liu 2010), different approaches of distributing the aerodynamic singularities (on an undeformable reference plane or attached to the body) as well as modeling of the wake (rigid or free) are evaluated. It will be shown that solvers implementing different assumptions may lead to considerably different results. This is especially true for Box-Wing like configurations, for which aerodynamic load redistribution has a major impact on aeroelastic performances: wake deformation is then a factor to take account of.

It is important to place this effort within an historical and bibliographical context. Flutter

analysis of Joined Wings was first performed in reference (Lange *et al.* 1974), for a box-wing layout (Miranda 1974). It was found that the flutter instability was a limitation to the design of the configuration. Later, (Divoux and Frediani 2012, DalCanto *et al.* 2012) the so called *PrandtlPlane* (Frediani 1999, Frediani 2002, Frediani 2003) configuration was studied on an aeroelastic perspective and the encountered flutter problems were alleviated with the introduction of a double fin. Also Weisshaar and Lee (2002) studied flutter properties of a diamond-wing layout. In all the above references linear flutter prediction methods were used. Moreover, the analyses were carried out on *realistic* (i.e., inertial and stiffness distributions were assessed considering real-like operative conditions) aircraft, whereas only conceptual investigations on wind tunnel-like models will be pursued in this paper.

However, linear results could be non-conservative since higher critical speeds may be predicted (see Demasi *et al.* (2013b)). If a large discrepancy between the linear and nonlinear predicted aeroelastic instability speeds is found on the conceptual models, then a *qualitative indication* on the actual aircraft is implicitly provided.

Very few results have been proposed for different layouts of Joined Wings (Bhasin 2012), and a lack of understanding of the underlying physics is evident: additional studies are then necessary.

3. Theoretical highlights of the present computational tools

In a generic aeroelastic code the basic aerodynamic and structural solvers need to interact, passing to each other the information regarding the deformations (which directly influence the aerodynamic forces) and the forces (which deform the structure). It goes well beyond the goals of this paper to present a summary of all the possible strategies that could be adopted. The authors refer the reader to excellent works as (Felippa and Geers 1988, Deparis *et al.* 2006, Küttler and Wall 2008) and the herein cited references.

In the following, the *components* of the in-house aeroelastic capabilities are described separately. They consist in a finite element method for the computational structural dynamics (CSD) and an unsteady vortex lattice method (UVLM) for the time-domain aerodynamic simulations. A doublet lattice method (DLM) for the frequency-domain unsteady aerodynamics calculations is also employed: details about this particular solver could be found in literature (Rodden *et al.* 1998, Demasi and Livne 2009b, Demasi and Livne 2009c).

Hereinafter, different interface (load/displacement transferring) strategies are analyzed. Finally, the different aeroelastic solvers are discussed.

3.1 Structural finite element model and dynamic solver

The geometrically nonlinear finite element (see Cavallaro *et al.* 2014a, and the therein cited references) is based on the linear membrane constant strain triangle (CST) and the flat plate discrete Kirchhoff triangle (DKT). The capability has also embedded the calculation of the structural tangent matrix $\boldsymbol{K}_T$, which is the sum of two contributions: the elastic stiffness matrix, $\boldsymbol{K}_E$, and the geometric stiffness matrix, $\boldsymbol{K}_G$. Composite materials are implemented. A corotational approach is used, and thus, rigid body motion is eliminated from elements and the pure elastic deformations are found.

The postcritical capabilities of the aeroelastic code are here omitted for brevity (see Cavallaro *et al.* 2013a, Demasi *et al.* 2013b for a thorough discussion). A detailed description of the dynamic

solver is presented in the extended conference version of this paper (Cavallaro *et al*. 2014b). On this regard, a large attention is devoted to the time-integration of the aeroelastic nonlinear equation within an energy-momentum conserving algorithm framework derived from Kuhl and Ramm (1999). Again, the reader is referred to the extended version of this paper (Cavallaro *et al*. 2014b) for more details regarding this specific topic.

3.2 Aerodynamic model

3.2.1 Introduction

The present section introduces the aerodynamic model adopted in the study. The hypotheses of potential and incompressible flow are assumed to be valid.

3.2.2 Geometry definition and evaluation of induced velocity

Unsteady Vortex Lattice Method (UVLM) is used as aerodynamic solver: the main advantage of such a formulation is the required small programming effort, which makes it preferable when operating with thin wings; for a detailed treatise refer to (Katz and Plotkin 2001).

The singularities are vortex ring elements, each of which is composed by four constant-strength vortex line segments with the same value of circulation Γ. The wing is discretized by an arbitrary user-selected number of quadrilateral aerodynamic panels as shown in Fig. 1.

The vortex ring associated with each panel is shifted downstream along each lateral edge of one fourth of the same edges. The velocity induced at an arbitrary point P by the generic vortex segment of circulation Γ is obtained from the Biot-Savart law. In particular, assume $\boldsymbol{V}_{\mathrm{SI_{km}}}$ to be the velocity induced in the k-th collocation (or control) point by the m-th ring of unitary circulation. Moreover, consider that the generic k-th collocation point (where the wall tangency condition has to be enforced) lies on the *center* of the k-th vortex ring, whose local direction is $\boldsymbol{n}_k$. Then, it is possible to define the generic km-th term of matrix of body influence coefficients $\boldsymbol{A}$

$$A_{\mathrm{km}} = \boldsymbol{V}_{\mathrm{SI_{km}}} \cdot \boldsymbol{n}_k \tag{3}$$

3.2.3 Wake model

For an unsteady flow a key role is played by the modeling of the wake. The most accurate

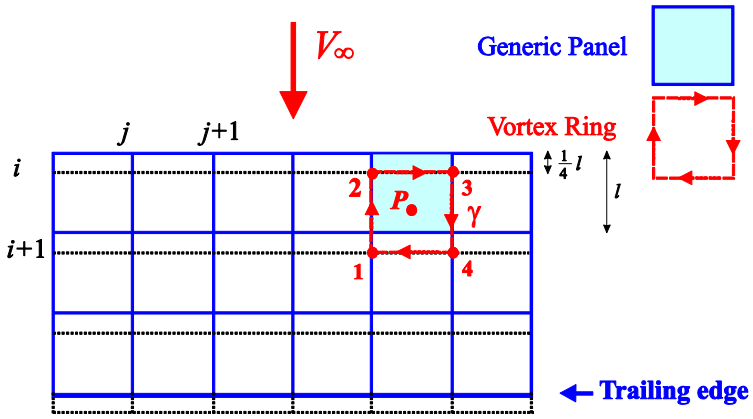

Fig. 1 Location of the vortex rings in the aerodynamic grid

model prescribes that each vortex moves with the local stream velocity since the vortex wake is force free (free wake), obtaining the so called *wake roll-up*. However this approach is quite time consuming and, thus, often the wake is considered as being simply convected by the freestream velocity (rigid wake). The effects of wake modeling on the aeroelastic responses will be discussed later.

In both cases, the wake is described with several rows of vortex rings of different strength, each shed at a certain time step. When impulsively starting from a rest condition, only wing bound vortex rings exist. Consequently, there are no wake panels and the solution is easily found by specifying the zero normal flow boundary condition on the collocation points. During the second time step, the wing moves along its flight path and each trailing edge vortex panel sheds a wake ring with vortex strength equal to its circulation in the previous time step (automatically satisfying the Kelvin condition). For the case of rigid wake, it is enough to impose that each wake's point is convected by the freestream velocity and so the procedure can be continued at each successive time step determining in such a way a wake of known geometry. Notice that, a wake vortex ring does not change its circulation (consequence of Helmholtz theorem).

If the free wake is modeled, at the end of each time step, once the problem is solved and the unknown intensity of the circulation Γ of every ring of the body is known, the evaluation of the induced velocity (u,v,w) at each vortex ring corner point l is performed in order to move the vortex elements by

$$(\Delta x, \Delta y, \Delta z)_l = (u, v, w)_l \cdot \Delta t \tag{4}$$

This is the only difference between the two methods, because once the wake geometry is defined, the calculation of influence matrices and thus, the solution of the problem at the next time step are established in an identical manner.

It is now possible to evaluate the contribution of each wake ring r-th to the local velocity in the k-th control point and create the $\boldsymbol{A}_w$ matrix of wake influence coefficients, where

$$\boldsymbol{A}_{w_{kr}} \cdot \boldsymbol{\Gamma}_w = \boldsymbol{V}_{\mathrm{WI}_{kr}} \cdot \boldsymbol{n}_k \tag{5}$$

being $\boldsymbol{V}_{\mathrm{WI}_{kr}}$ the wake-induced velocity from wake ring r at the collocation point k.

Details on the desingularization techniques necessary for regularizing the vortex inductions can be found in the extended conference version of this work (see Cavallaro *et al*. 2014b).

3.2.4 Boundary condition

To write the wall tangency condition, all the contributions have to be taken into account: the velocity induced by the body rings $\boldsymbol{V}_{\mathrm{SI}}$ and wake rings $\boldsymbol{V}_{\mathrm{WI}}$, the kinematic velocity $\boldsymbol{V}_{\mathrm{KIN}}$ which is the velocity of wind on the surface (in particular at the collocation points) due to relative motion of the wing, as viewed in the body frame of reference. This last contribution depends on the freestream velocity, the rigid motion of the body but also on the elastic deformation of the body $\boldsymbol{V}_{\mathrm{rel}}$ (this is relevant in aeroelastic problems). The terms $\boldsymbol{V}_{\mathrm{WI}}$ and $\boldsymbol{V}_{\mathrm{KIN}}$ contribute to the right hand side, whereas $\boldsymbol{V}_{\mathrm{SI}}$is unknown (product of the multiplication of matrix $\boldsymbol{A}$ of Eq. (3) with the unknown intensity of the body vortex rings). Thus, it is possible to write in a matrix form the following system

$$\boldsymbol{A} \cdot \boldsymbol{\Gamma} = \boldsymbol{RHS} \tag{7}$$

where $\boldsymbol{\Gamma}$ is the array containing the unknowns (strength of the vortex rings), and

$$RHS_k = -(\boldsymbol{V}_{\mathrm{WI}_k} + \boldsymbol{V}_{\mathrm{KIN}_k}) \cdot \boldsymbol{n}_k \tag{8}$$

is the vector containing the known part of the normal velocity components.

3.3 Interface algorithm

In this section only the moving least square (MLS) approach is described. The aeroelastic framework also has implemented the infinite plate spline (IPS) method: details on this formulation can be found in Harder and Desmarais (1972).

3.3.1 Interface with moving least square derived algorithm

The present interface algorithm has the purpose to solve the typical aeroelastic problem of coupling the aerodynamic and structural meshes granting important features (Quaranta *et al.* 2005). It is in fact possible to interface both non-matching surfaces and non-matching topologies. Cases in which a control point falls outside the range of the source mesh are also naturally tackled. Moreover, there is a relative insensitiveness to the node density variations in the source mesh.

A very important feature is the conservation of exchanged quantities, in particular momentum and energy: this is a keypoint since in literature (Cebral and Lohner 1997) it has been shown how nonconservative interfaces may lead to wrong results. In spite of these valuable advantages, the efficiency of interface computation is high.

Traditionally, *meshless* methods were introduced as a method of numerical resolution of partial differential equations different than finite element method (FEM), finite difference method (FDM) and finite volume method (FVM). In these last approaches, spatial domain is often discretized into meshes: the set of differential equations are approximated by a set of algebraic equations for each mesh and then, by appropriately assembling all contributions, the final system of algebraic equations for the whole problem is obtained. On the contrary, in mesh free method (Liu 2010), this system of algebraic equations for the whole problem is obtained using a set of nodes scattered in the domain which do not form a mesh because no information on the relationship between the nodes (e.g., connectivity of an element) is required.

These methods seem to solve some issues of the classical approaches which are here briefly listed. First, the creation of an adequately discretized mesh is notoriously a bottleneck in the process since it is both manpower and computer time consuming. Second, the classical approaches have a limited regularity of the solution, especially in its derivatives, at the elements' boundaries (although approaches using higher order continuous basis function like *NURBS* were already proposed, e.g., Celniker and Gossard 1991). Moreover, with Lagrangian grids/meshes there is a loss of accuracy when large deformations are investigated because of the element distortion. A close examination of these difficulties shows that the root of the problem is the necessity to use elements (mesh); on the contrary a meshless method does not have these limitations, and could add or delete nodes when they are needed, providing a great flexibility to the analysis.

In the present effort what is inherited from the *meshless* method is one of its central features: the shape functions. A number of ways to construct shape functions has been proposed in literature; here the choice falls on Moving Least Square approximation (MLS), which belongs to the family of finite series representation methods. This family of shape functions was originally introduced for data fitting and surface reconstruction (see Lancaster and Salkauskas 1981), while in Nayroles *et al.* (1992) they were used for the first time to build shape functions for the Diffuse Element Method (DEM), which was among the first ones to be properly called *mesh free method*, and had a strong impact on the field. The two main features of MLS are the continuity and smoothness in the problem domain of the approximated field function, and the ability to produce

the desired order of consistency (a method is said to be *k*-th order consistent if it can reproduce polynomials of up to the *k*-th order). The procedure of constructing shape functions using MLS approximation is fully presented in Cavallaro *et al.* (2014b).

3.4 Aeroelastic coupling

In this section the goal is to express the aerodynamic loads in order to formulate the aeroelastic problem.

3.4.1 Boundary condition

The starting point to obtain the sought expression is the boundary condition (enforced at the control points).

Recalling the matrix formulation from Eq. (7), it is worth to highlight the various contributions to the $\boldsymbol{RHS}$ vector. The *first* contribution can be written as

$$\boldsymbol{RHS}_1 = -\boldsymbol{A}_w \cdot \boldsymbol{\Gamma}_w \tag{9}$$

where $\boldsymbol{A}_w$ is the wake influence coefficients matrix and $\boldsymbol{\Gamma}_w$ is the vector with the strength of the wake singularities, both completely defined from the previous time steps calculations.

The *second* term is the freestream contribution

$$\boldsymbol{RHS}_2 = -\boldsymbol{V}_\infty^n \tag{10}$$

where $\boldsymbol{V}_\infty^n$ is the component of the freestream velocity along the normal to the ring. In order to evaluate this term, it is useful to consider Fig. 2, in which the *k*-th body ring, the position of the associated control point, and a sketch of both the deformed and undeformed configurations are depicted. Unit vector $\boldsymbol{i}$ is parallel to the free stream, while $\boldsymbol{i}^S$ is the direction of the free stream projected to the undeformed ring plane. By definition, the *k*-th element of $\boldsymbol{V}_\infty^n$ is given by $V_\infty \boldsymbol{i} \cdot \boldsymbol{n}_k$, where $\boldsymbol{n}_k$ is the normal to the ring in its *actual* configuration, and the following holds

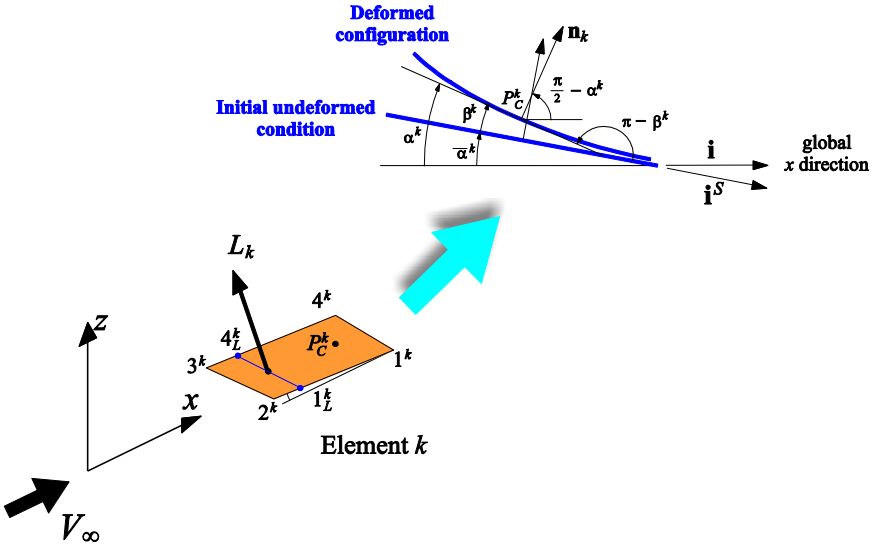

Fig. 2 Geometry and local normal of the body ring

$$\boldsymbol{i}\cdot\ \boldsymbol{n}_k = \cos\left(\frac{\pi}{2} - \alpha^k\right) = \sin\left(\alpha^k\right) = \sin\left(\overline{\alpha^k} + \beta^k\right) = \sin(\overline{\alpha^k})\cos(\beta^k) + \cos(\overline{\alpha^k})\sin(\beta^k) \quad (11)$$

being $\overline{\alpha^k}$ the angle of attack of ring *k* in the undeformed configuration and the angles α^k and β^k the ones reported in Fig. 2.

Under the assumption of small angles:

$$\cos\left(\overline{\alpha^k}\right) \approx 1$$

$$\cos\left(\beta^k\right) \approx 1$$

$$\sin\left(\beta^k\right) \approx \tan\left(\beta^k\right) = -\tan\left(\pi - \beta^k\right)$$

A synthetic expression of Eq. (10) can be given, discerning the different meanings of the involved terms

$$V_\infty \boldsymbol{i}\cdot\ \boldsymbol{n}_k = V_{\infty,0}^{n_k} + V_{\infty,d}^{n_k} \quad (12)$$

Where $V_{\infty,0}^{n_k} = V_\infty \sin(\overline{\alpha^k})$ is the *k*-th element of $\boldsymbol{V}_{\infty,0}^{n}$, and is related to just the change in the rigid angle of attack (*rigid angle of attack*); it is thus a function of the time only.

The second term $V_{\infty,d}^{n_k}$ is the contribution of the free stream due to the deformation of the wing (*elastic angle of attack*) and is a function of the deformed shape. Observing that $\tan\left(\beta^k\right)$ is equal to the opposite of the derivative of control point's displacement in the direction of the *undeformed* normal in respect to the direction $\boldsymbol{i}^s$ (*undeformed x* direction), it can be written

$$V_{\infty,d}^{n_k} = -V_\infty \frac{d\widehat{Z_k}}{dx_k^S} \quad (13)$$

where the vector $\widehat{\boldsymbol{Z}}$ collects the displacements of the control points along the undeformed aerodynamic rings' normals. This contribution can be directly related to the slope of the normal component of displacement of the control point *k*.

The third term $\dot{\boldsymbol{Z}}$ originates from the relative body-flow velocity that is established as the body changes its shape/position, giving a contribution to the effective flow speed that has to be taken into account for a correct evaluation of Eq. (10). This is an important source of aerodynamic damping. It holds

$$\boldsymbol{RHS}_3 = \dot{\boldsymbol{Z}} \quad (14)$$

The generic $\dot{\boldsymbol{Z}}$ can be evaluated extrapolating the deformation velocity on the control points from the vector $\dot{\boldsymbol{U}}$, which contains the generalized velocity of the structural nodes, and multiplying it by the normal to the *k*-th ring $\boldsymbol{n}_k$, in its *actual* configuration.

Now that all the RHS terms have been conveniently rearranged, Eq. (7) can be reformulated as

$$\boldsymbol{A}\cdot\boldsymbol{\Gamma} = \boldsymbol{RHS}_1 + \boldsymbol{RHS}_2 + \boldsymbol{RHS}_3 = -\boldsymbol{A}_w\cdot\boldsymbol{\Gamma}_w - \boldsymbol{V}_\infty^n + \dot{\boldsymbol{Z}} \quad (15)$$

and, inverting $\boldsymbol{A}$, this final equation is obtained

$$\boldsymbol{\Gamma} = \boldsymbol{\Gamma}_1 + \boldsymbol{\Gamma}_2\cdot\boldsymbol{U} + \boldsymbol{\Gamma}_3\cdot\dot{\boldsymbol{U}} \quad (16)$$

$\boldsymbol{\Gamma}_1$ is the known contribution due to the wake and to the *rigid angle of attack*, i.e., the first term in Eq. (12)

$$\boldsymbol{\Gamma}_1 = -\boldsymbol{A}^{-1}\boldsymbol{A}_W\cdot\boldsymbol{\Gamma}_w - \boldsymbol{A}^{-1}\boldsymbol{V}_{\infty,0}^n \quad (17)$$

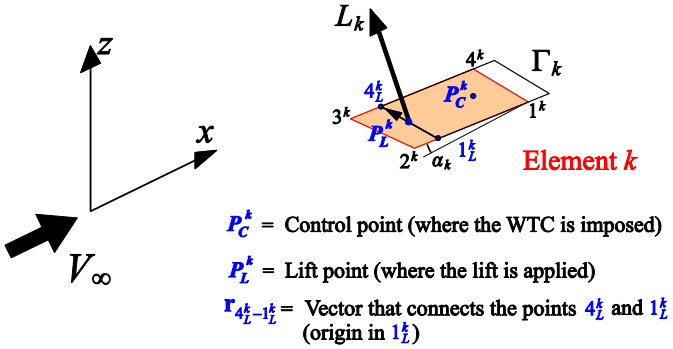

Fig. 3 Direction of the lift over the ring *k*

$\boldsymbol{\Gamma}_2$ is the matrix that multiplies the displacement field $\boldsymbol{U}$; it features a matrix ($\boldsymbol{H}_{\mathrm{dx}}$) performing the interpolation between the aerodynamic and structural meshes in order to get the derivative with respect to x_k^S of the displacement. This matrix is multiplied by matrix $\boldsymbol{N}_0$ in order to sample correctly just the component parallel to the *undeformed* normal of the ring

$$\boldsymbol{\Gamma}_2 = -V_\infty \boldsymbol{A}^{-1} \boldsymbol{N}_0 \boldsymbol{H}_{\mathrm{dx}} \tag{18}$$

$\boldsymbol{\Gamma}_3$ multiplies the given velocity field $\dot{\boldsymbol{U}}$. The $\boldsymbol{H}_{\mathrm{disp}}$ matrix performs the interpolation between the two meshes, and is multiplied by ($\boldsymbol{N}_{\mathrm{d}}$) in order to correctly sample just the component parallel to the *actual* normal to the ring.

$$\boldsymbol{\Gamma}_3 = \boldsymbol{A}^{-1} \boldsymbol{N}_{\mathrm{d}} \boldsymbol{H}_{\mathrm{disp}} \tag{19}$$

3.4.2 Aeroelastic loads

Starting from the Bernoulli equation for an incompressible, irrotational and unsteady flow, and following reference Katz and Plotkin (2001) it is possible to evaluate the aerodynamic actions. These relations can be advantageously expressed in matrix form as

$$\boldsymbol{p} = \rho \boldsymbol{\Delta} \cdot \boldsymbol{\Gamma} + \rho \frac{\partial \boldsymbol{\Gamma}}{\partial t} \tag{20}$$

where $\boldsymbol{p}$ is the array containing the difference between upper and lower pressure for each panel, $\boldsymbol{\Delta}$ is the matrix that, for each ring of the body, applies the finite difference derivative scheme to $\boldsymbol{\Gamma}$ and multiplies it with the suitable coefficients. To finally obtain the expression of the lift acting on the load points of the aerodynamic mesh, the direction $\boldsymbol{r}_L^k$ of the force over the *k*-th ring is chosen accordingly to the Kutta-Joukowsky theorem as

$$\boldsymbol{r}_L^k = \boldsymbol{i} \times \boldsymbol{r}_{4_L^k - 1_L^k} \tag{21}$$

where $\boldsymbol{r}_{4_L^k-1_L^k}$ connects the projections of the load point P_L^k along the segments $3^k - 4^k$ and $2^k - 1^k$ (as depicted in Fig. 3) and has a magnitude equal to the width of the ring panel.

Calling c_k the chord of the ring and ($\boldsymbol{i}, \boldsymbol{j}, \boldsymbol{k}$) the axes direction in the global coordinate system, a general expression of the three components of the lift force acting on the k^{th} ring is finally given

$$
\begin{aligned}
L_x^k &= c_k \;\; \boldsymbol{i} \cdot \boldsymbol{r}_{4_L^k - 1_L^k} p_k \\
L_y^k &= c_k \, \boldsymbol{j} \cdot \boldsymbol{r}_{4_L^k - 1_L^k} p_k \\
L_z^k &= c_k \;\; \boldsymbol{k} \cdot \boldsymbol{r}_{4_L^k - 1_L^k} p_k
\end{aligned}
\tag{22}
$$

which in matrix form becomes

$$\boldsymbol{L} = \boldsymbol{S} \cdot \boldsymbol{p} \tag{23}$$

If N is the number of body rings, $\boldsymbol{S}$ is a $3N \times N$ matrix such that, when multiplied by $\boldsymbol{p}$, gives rise to vector $\boldsymbol{L}$, whose dimensions are $3N \times 1$, and is assembled repeating the pattern of Eq. (22) for each element k.

As it can be inferred from Eq. (20), the unsteady part of the pressure depends on the derivative of $\boldsymbol{\Gamma}$ with respect to time. The derivation can be carried out using Eq. (16), leading to

$$\frac{\partial \boldsymbol{\Gamma}}{\partial t} = \frac{\partial \boldsymbol{\Gamma_1}}{\partial t} + \boldsymbol{\Gamma}_2 \cdot \dot{\boldsymbol{U}} + \boldsymbol{\Gamma}_3 \cdot \ddot{\boldsymbol{U}} \tag{24}$$

where the derivatives of $\boldsymbol{\Gamma}_1$, $\boldsymbol{\Gamma}_2$, and $\boldsymbol{\Gamma}_3$ are assumed negligible (future work will precisely assess the effects of these derivatives with additional test cases and simulations). Now Eq. (20) combined with Eqs. (16) and (24) lead to the sought expression for the aerodynamic loads

$$\boldsymbol{L}^{\mathrm{LP}} = \boldsymbol{L}_1^{\mathrm{LP}} + \boldsymbol{L}_2^{\mathrm{LP}} \cdot \boldsymbol{U} + \boldsymbol{L}_3^{\mathrm{LP}} \cdot \dot{\boldsymbol{U}} + \boldsymbol{L}_4^{\mathrm{LP}} \cdot \ddot{\boldsymbol{U}} \tag{25}$$

With

$$
\begin{aligned}
\boldsymbol{L}_1^{\mathrm{LP}} &= \rho \boldsymbol{S} \cdot \Delta \cdot \boldsymbol{\Gamma_1} \\
\boldsymbol{L}_2^{\mathrm{LP}} &= \rho \boldsymbol{S} \cdot \Delta \cdot \boldsymbol{\Gamma_2} \\
\boldsymbol{L}_3^{\mathrm{LP}} &= \rho \boldsymbol{S} \cdot \Delta \cdot \boldsymbol{\Gamma_3} + \rho \boldsymbol{S} \cdot \boldsymbol{\Gamma_2} \\
\boldsymbol{L}_4^{\mathrm{LP}} &= \rho \boldsymbol{S} \cdot \Delta \cdot \boldsymbol{\Gamma_3}
\end{aligned}
$$

The superscript LP is used to remind that these forces are applied on the load points of the rings. As for the matrices $\boldsymbol{H}_{\mathrm{dx}}$ and $\boldsymbol{H}_{\mathrm{disp}}$, the interface algorithm will provide the way to transfer these quantities to the structural nodes.

3.5 Aeroelastic solvers

Three solvers have been used in the present study. Each of them is characterized by using different options both on the pure aerodynamic side (but within the model of incompressible potential flow), and on the aeroelastic coupling. The three solvers, called *Solver1*, *Solver2* and *Solver3* have increasing computational cost. Their properties are graphically presented in Fig. 4. A solver based on the *doublet lattice method* (DLM, see Rodden *et al.* 1998) is occasionally employed for comparison purposes.

3.5.1 Solver 1

This model adopts the IPS as interface algorithm; this implies simplified hypotheses, inherent both to the limits of the algorithm itself and to simplifications needed to preserve low computational costs. As a consequence the aerodynamic mesh *does not* follow the structure, i.e., the coordinates of rings and the control points, employed in the evaluation of the coefficients of

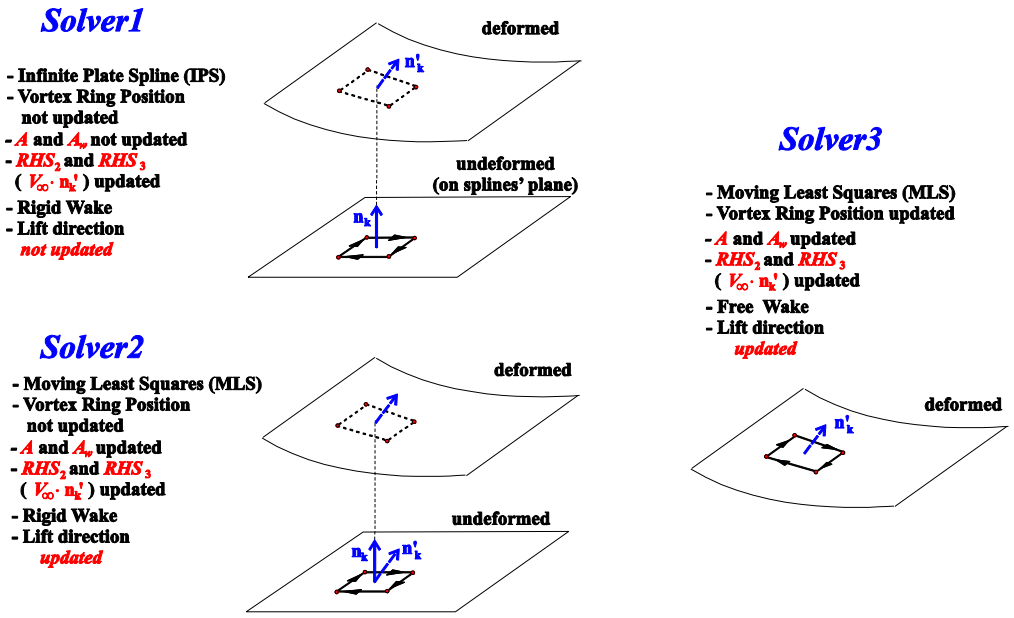

Fig. 4 Differences between the time-domain aeroelastic solvers

the matrices $\boldsymbol{A}$ and $\boldsymbol{A}_w$ (see section 3.2.2 and 3.2.3) do not depend on the deformation process of the body. However, body's deformation still influences the boundary condition (and thus the aerodynamic loads) with the terms $\boldsymbol{RHS}_2$ and $\boldsymbol{RHS}_3$ discussed in section 3.4.1. Such a choice implies that a rigid wake model is adopted.

3.5.2 Solver 2

In *Solver2* MLS interpolation algorithm is used (instead of IPS as in *Solver1*) to handle the coupling of aerodynamic and structural fields. Since MLS removes the obstacle of passing information between two sets of points occupying the same planar surface, as necessary with IPS, it possible to build up, for each time step, the real aerodynamic mesh.

However, in this case a mixed approach is chosen: the *velocity vector* used for the matrices $\boldsymbol{A}$ and $\boldsymbol{A}_w$ is still evaluated ignoring the new position of the body, but the *aerodynamic coefficients* of these matrices (i.e., the normal components of the velocities) are updated at each time step because in Eqs. (3) and (5) it is considered the actual normal direction $\boldsymbol{n}_k$ of the ring.

The reason of this choice is the assumption that for a correct estimate of the *velocity vector* the important aspect is the relative distance between the vortex line and the induced point and this is still in good agreement with the initial one when the body is deformed. On the contrary, what is mainly changed during the dynamic evolution, especially for very deformed configurations as the ones under investigation, is the direction along which the boundary condition should be written. Thus, there is a lack of accuracy in keeping projecting the induced velocity vector on the initial normal direction.

Thanks to the MLS is possible to evaluate the updated $\boldsymbol{r}_L^k$, which gives the direction of lift produced by the *k*-th ring, see Eq. (21), by simply considering the actual position of the points $4_L^k$and 2_L^k of Fig. 3. It is worth to notice that now the aerodynamic load is *follower both in direction and magnitude.*

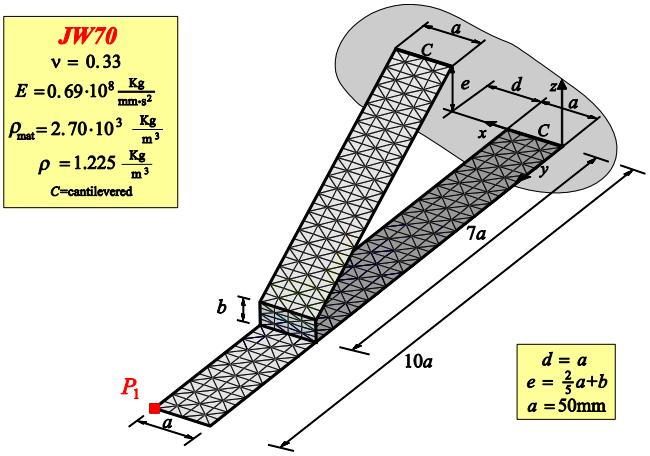

Fig. 5 JW70 model. The joint is located at 70% of the wingspan. The thickness of the different parts of the structure is equal to 0.7 mm

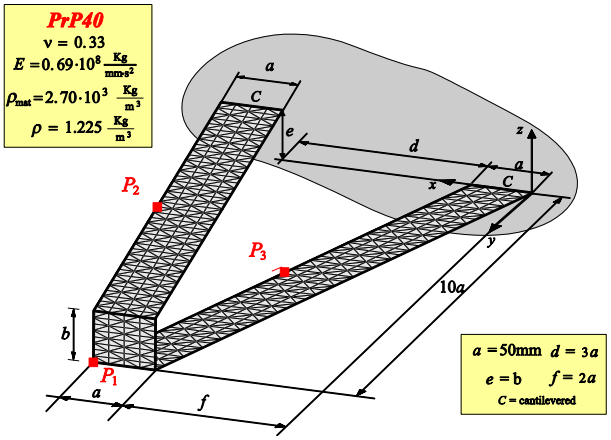

Fig. 6 PrandtlPlane Joined Wing model PrP40. The joint is located at the tip of the wings

Since the aerodynamic mesh still remains attached to the *undeformed* configuration, free-wake approach has been not considered to be meaningful, thus, *Solver2* represents an improvement in the accuracy comparing to the *Solver1* without an excessive drawback in simulation run time.

3.5.3 Solver 3

Solver3 adopts the MLS interpolation algorithm and considers the aerodynamic mesh in its actual position, enabling the free-wake model and the *correct* (without further assumptions as the ones made before) expression of all the quantities involved in the evaluation of the aerodynamic loads.

3.6 Validation of the computational capability

Validation of the in-house computational capabilities can be found in previous works (Cavallaro *et al.* 2013a, Cavallaro *et al.* 2014b, Demasi and Livne 2009a).

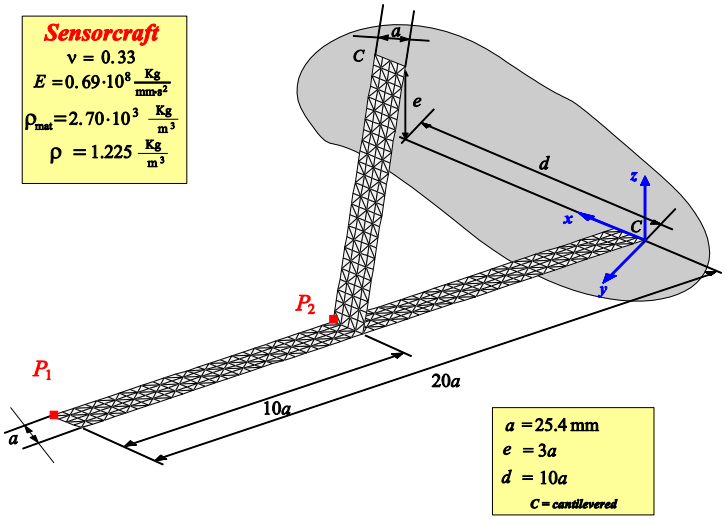

Fig. 7 *Sensorcraft*. The aft wing is connected to the front one at the mid-span. The thickness of the wings is equal to 0.7 mm.

4. Description of the analyzed joined-wing configurations

There are different configurations that will be analyzed in this paper. The first one, depicted in Fig. 5, is a Joined Wing (named *JW70*) in which the joint is not located at the tip of both the wings. The thickness of the wings and the joint is 0.7 mm.

The second configuration (Fig. 6) is a PrandtlPlane-like (Frediani *et al.* 2012) configuration featuring a swept-back lower wing and a swept-forward upper wing. It is called *PrP40*. For this layout, the thickness of the wings is varied and specified case by case. Both *JW70* and *PrP40* have been chosen for reference reasons, see (Demasi *et al.* 2013a, Cavallaro *et al.* 2013a, Demasi *et al.* 2013b, Cavallaro *et al.* 2014a). The models' dimensions are selected to be consistent with the ones corresponding to wind-tunnel scaled models.

The last layout (Fig. 7) resembles the *SensorCraft* (Lucia 2005). The geometrical details are taken from reference (Patil 2003), apart from the thickness which has been set to 0.7 mm. In this configuration the aft wing is directly joined to the front wing, to act like a strut.

For all the layouts the adopted material is a typical aluminium, featuring a Young's modulus $E = 6.9 \cdot 10^7 \frac{\text{kg}}{\text{mm} \cdot \text{s}^2}$, a Poisson's ratio $\nu = 0.33$ and a density $\rho_{mat} = 0.69 \cdot 10^3 \frac{\text{kg}}{\text{m}^3}$.

For the aerodynamic analysis, the surface is discretized employing different (usually about 12) elements in the chordwise direction. The overall number of trapezoidal elements is then between approximately 600 and 3000 for the different cases.

Air density is relative to the standard air ($\rho = 1.225 \ \frac{\text{kg}}{\text{m}^3}$).

5. Snap-Divergence

The concept of *snap-divergence* was first introduced in Demasi *et al.* (2013b). It was related to a precise mathematical event, which was the singularity of the aeroelastic tangent matrix. For that

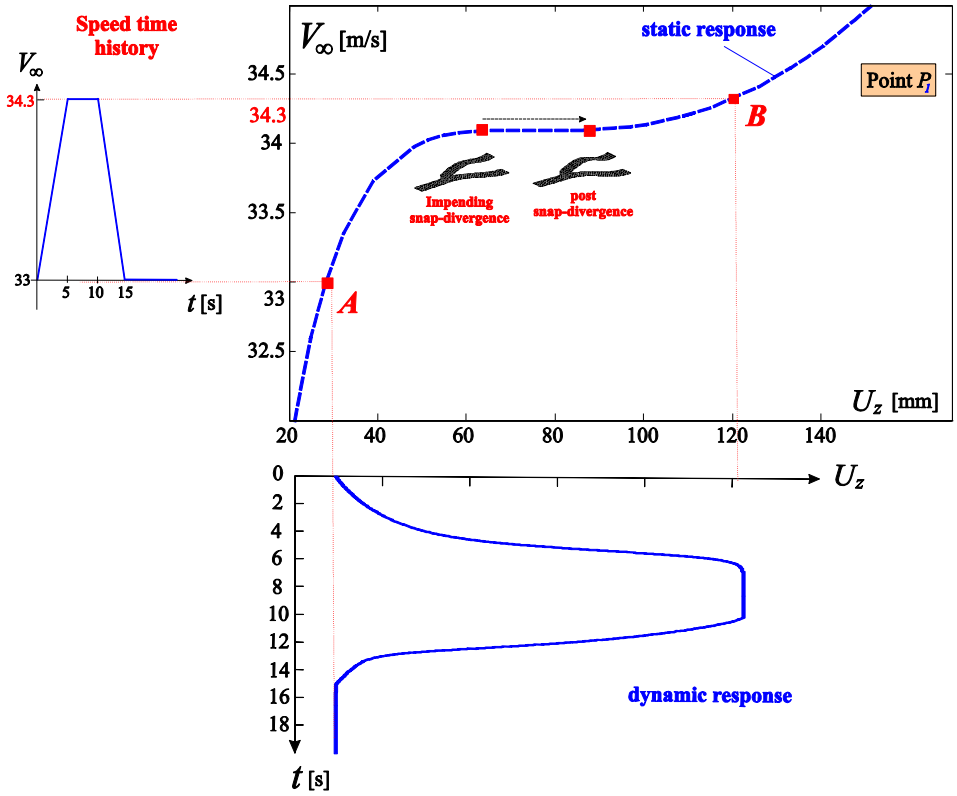

Fig. 8 Aeroelastic static response of *JW70*, speed-time history, and associated aeroelastic dynamic evolution. *Uz* refers to the vertical displacement of the wing tip, point *P*1 of Fig. 5

critical condition an infinitesimal increment in the onset flow speed determined an equilibrium state not continuously adjacent to the previous one. In other words, a jump phenomenon (from which the word *snap*) was expected.

This jump phenomenon could be theoretically demonstrated to happen if the acting forces are of the conservative type, and this actually is pursued and shown in Cavallaro *et al.* (2013a). However, aerodynamic forces are not of the conservative type and the scenario could be much more complicated.

First of all, for the here investigated case it has been verified that flutter speed is larger than snap-divergence one, thus, the stability (in a local sense) of the equilibrium points could be assessed with static aeroelastic analysis. However, different-than-fixed point type of attractors may theoretically exist, with the consequence that snap may induce the system to settle, for example, to a limit cycle oscillation.

In this section the snap-divergence response will be shown. The time-domain capability is used, in particular *Solver1*. This choice is dictated by the necessity to keep the aeroelastic modeling consistent to the one used in reference (Demasi *et al.* 2013b).

5.1 Time response on snap-divergence occurrence

Consider the static aeroelastic response reported in Fig. 8 (taken and adapted from Demasi *et*

al. 2013b). Starting from the steady state A, the flow speed was changed as described in the following.

It is worth to explain how the simulation was started. The steady state aeroelastic solver was using horse shoe singularities to represent the bound vorticity, whereas in the time-domain capability a vortex ring representation is used. Equivalence has been imposed on the aerodynamic loads, determining thus the circulation of the vortex rings. A further point is the fact that static solutions were considered converged after a tolerance on the residual was reached. Of course, in a real numerical setting it is not possible to reach the perfect equilibrium. Thus, it has been checked that the numerical unbalance was negligible.

Given the initial condition (state *A* in Fig. 8, corresponding to a freestream speed of $V_\infty = 33\ \mathrm{m/s}$) the flow speed is first increased to reach $V_\infty = 34.3\ \mathrm{m/s}$ (state *B*), then decreased to its initial value. This is a quasi-static process, as could be inferred from the box in Fig. 8, where the wind speed in respect of time is plotted.

Tracking the dynamic response, as long as the speed approaches values close to the one of *snap-divergence*, there is an abrupt increase in the displacement of the wing tip (measure of the deformation of the structure). Comparing the displacements for the static and dynamic cases, the snap-divergence phenomenon may be well recognized. In the inverse phase, where the speed is decreased to its initial value, similar trend is observed and the initial static equilibrium condition is obtained at the end of the transient. Further looking at the response, the inertial effects seem to be of secondary importance in this specific case, in fact no oscillation is observed.

Summarizing, the dynamic response matches closely the static one.

6. Flutter evaluated with linear and nonlinear analyses

This section shows how linear and nonlinear tools may predict notably different flutter speeds. As outlined in section 3, the here considered nonlinearities are relative to large displacements of the configurations (geometric nonlinearities). Similar comparisons were already pursued in publications (Demasi *et al.* 2013a, Demasi *et al.* 2013b), for mechanical loading and static aeroelastic conditions, respectively. It was assessed that linear analysis might give unreliable and nonconservative predictions. In some cases linear tools were not even able to correctly evaluate trends when one or more parameters were varied.

In this section differences between the two approaches from an aeroelastic dynamic point of view are tracked by means of the frequency-domain (DLM) solver (Demasi and Livne 2009b). This solver requires the modes of the structure (and also the generalized stiffness matrix) as an input. Thus, as it will be shown, running different analyses with modes representative of undeformed or deformed structure is how nonlinear effects are introduced.

6.1 PrP40

The configuration *PrP40* is first taken into consideration. The thickness of the structure is set to $t = 1\ \mathrm{mm}$. Evaluating the modal properties of the structure at different points on the static aeroelastic response (the static aeroelastic equilibrium states can be found in reference Demasi *et al.* 2013b and are presented also in the next session), it is possible to have a progressively more refined estimate of the flutter speed (Hopf's bifurcation).

Results (see Fig. 9) are relative to different values of damping ratio ζ.

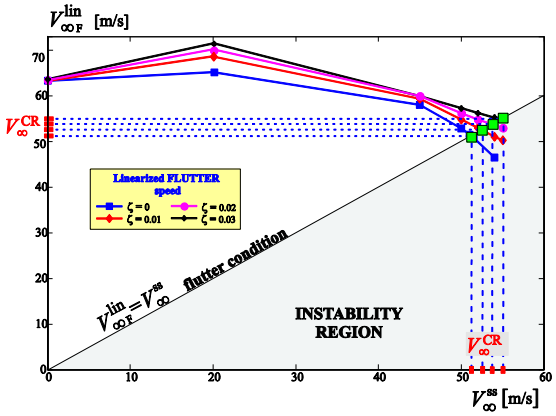

Fig. 9 Flutter speed predicted linearizing about steady state relative to different flow speeds for *PrP40*. The real critical condition (*nonlinear flutter*) occurs when these two speeds coincide

Flutter speeds are $51.5\ \mathrm{m/s}$ for the zero damping case, $52.2\ \mathrm{m/s}$ when $\zeta = 0.01$, $53.7\ \mathrm{m/s}$ when $\zeta = 0.02$ and $54.9\ \mathrm{m/s}$ when $\zeta = 0.03$. Discrepancy on flutter speed evaluated for the undeformed configuration (which is the common practice) and the real one is about 22%. Unfortunately, in this case the discrepancy is on the nonconservative side (overprediction of the critical condition).

Actually, increasing the linearization speed enhances this mismatch, at least for a large portion of the response. Interestingly enough, an overprediction of the divergence speed was also found for the aeroelastic static case (see Demasi *et al.* 2013b).

In literature it is claimed (Murua *et al.* 2012) that DLM model lacks in precision when used for cases in which wake roll-up plays an important role, or for cases in which the structural deformation is conspicuous. In other works (Attar *et al.* 2004) the real wake geometry was judged to be not influent for the specific aeroelastic case under examination. In this regard, next sections will present a comparison among flutter speeds predicted with different approaches (frequency vs. time-domain) and models.

6.2 Sensorcraft

Here the *Sensorcraft* is considered. Results are shown in Fig. 10. As it could be appreciated, there is still a non-negligible overprediction of the linear tool. In fact, considering the zero-damping case, the linear prediction gives $59.1\ \mathrm{m/s}$ against $51.6\ \mathrm{m/s}$, with a difference of approximately 15%. This is even more relevant considering the relatively smaller deformation associated with this configuration.

A further aspect to underline is the relative insensitiveness of the flutter speed in respect of the structural damping. This was not the case for the previously examined configuration (see Fig. 9).

It is interesting to observe that, linearizing about a speed other than the fundamental (zero) one, the flutter prediction instead of being more precise, may actually lead to larger errors. This was observed also for the *PrP40* case, suggesting that, evaluation done with immediate successive linearization may give misleading trends and even more inaccurate predictions, unless the linearization speed is close to the real critical one. These results stress out the relevant role played by the nonlinearities in Joined Wings configurations.

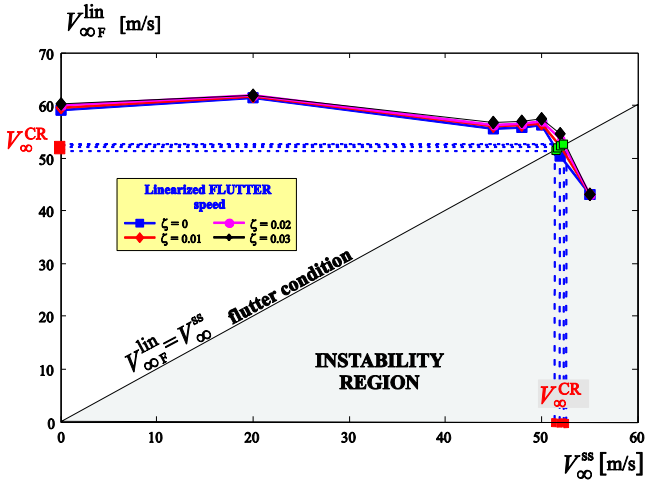

Fig. 10 Flutter speed predicted linearizing about steady state relative to different flow speeds for *Sensorcraft*. The real critical condition (*nonlinear flutter*) occurs when these two speeds coincide

7. Postcritical dynamical aeroelastic analysis

In this section different results are shown. Flutter speeds as predicted by the time- and frequency-domain solvers are compared, for different values of the damping ratio. For the post-flutter, different dynamic responses (in particular Limit Cycle Oscillations, LCO), are observed for the baseline configurations. These LCOs are obtained by perturbing the steady state, or, alternatively, by increasing the angle of attack until the target value is reached.

The discrepancies observed when different solvers are employed are discussed in more depth and a physical interpretation of these differences is also attempted, when possible. The outcome of this analysis has important consequences since it suggests which solver should be used to reach a good balance between reliability and computational costs.

7.1 Limit cycle oscillation for JW70

7.1.1 Solver 1

Fig. 11 shows the dynamic response of the *JW70* configuration evolving from an equilibrium state as the ones depicted in the graph. For each case, a vanishing perturbation of angle of attack is given to provoke a more observable transient, and eventually induce more rapidly a post-flutter behavior. This perturbation consists in a linear increase in the angle formed by the onset flow direction and the *x*-axis (α_x), followed by a symmetric decrease to the unperturbed value (which is $\alpha_x = 1°$). The peak is reached at 0.1 seconds, when it holds that $\alpha_x = 1.01$ (as shown in the box in Fig. 11).

No structural damping was considered. The simulations have been carried out at different speeds, so that both the typical subcritical and supercritical responses could be appreciated. In particular, with this approach, it is possible to locate a small interval in which the flutter speed lies (according to this solver). For the present case, the flutter speed falls in the interval $39.5 \div 40$ m/s. These results are analyzed and discussed in more depth in section 7.1.4.

For speeds larger than the one corresponding to flutter, an LCO is observed. The properties of

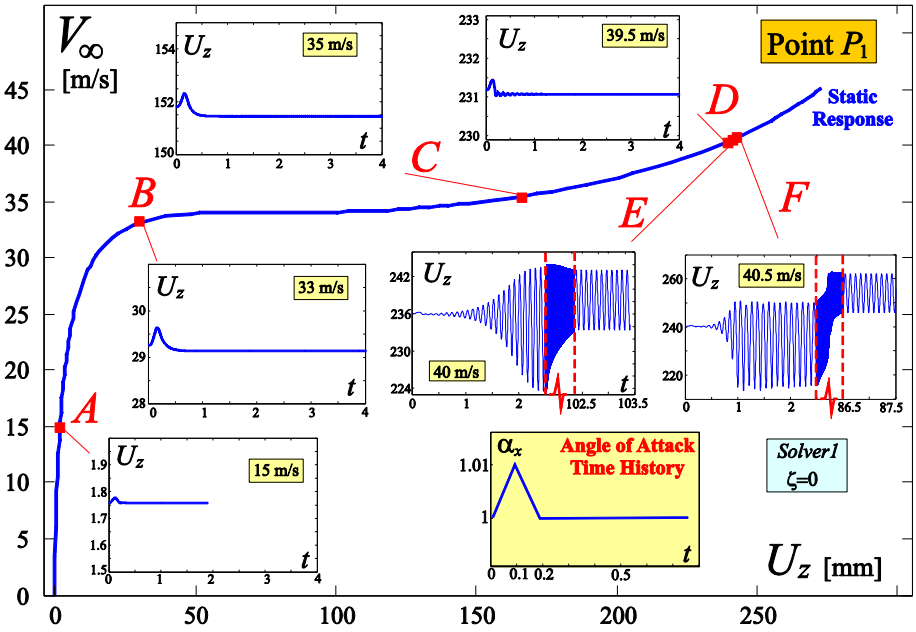

Fig. 11 *Solver1*. Aeroelastic dynamic response of *JW70* starting from steady states relative to different velocities when a vanishing perturbation of angle of attack of the onset flow is given

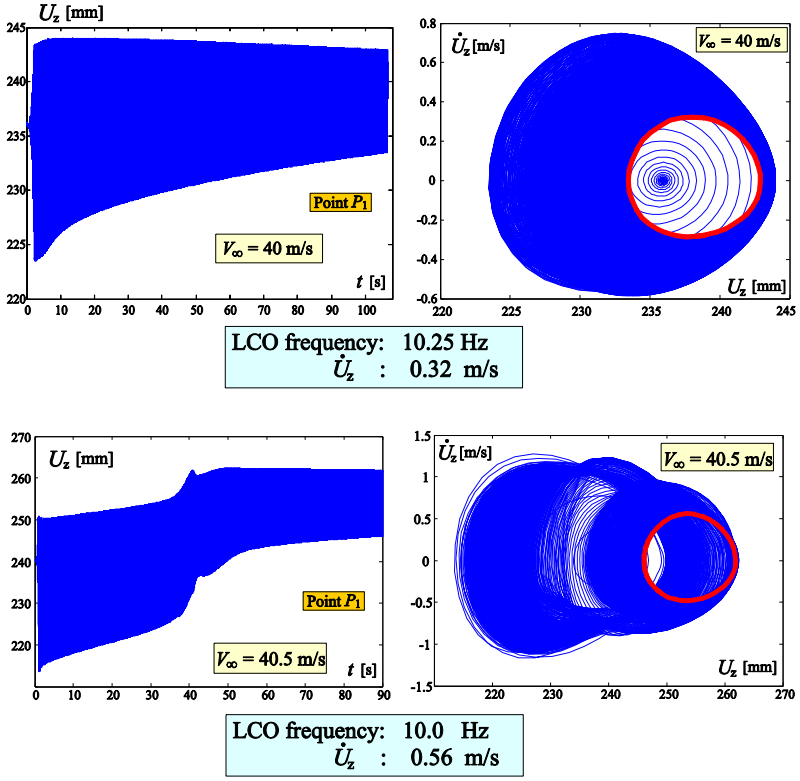

Fig. 12 Time response and phase-space trajectory for *JW70* configuration, for different flow speeds. *Solver1* is employed. No structural damping is considered

the LCOs are depicted in Fig. 12. Very interesting is the transient before settling to an LCO. Not only is the path described in the phase-space long before it is finally attracted from the LCO orbit, but, for a wind speed of $V_\infty = 40.5\ \mathrm{m/s}$ it has also an abrupt change in the oscillatory trend. It is the authors' opinion, and actually, it may be supported by physical sense, that this behavior is largely due to the overconstrained nature of the joined-wing layout. The mutual loads transferred through the joints give raise to a complicate response. This could be easily verified comparing the transient to the LCO shown above with the ones of the Delta Wing case (see reference Demasi and Livne 2009a).

7.1.2 Solver 2

The same process outlined in the previous section is now repeated using a different aerodynamic solver. The difference with the previous case is concentrated in a more consistent application of the boundary condition (which requires the re-evaluation of the aerodynamic tangent matrix at each time step) and also the application of the Kutta-Joukowsky formula on the real deformed structure. Moreover, all the aerodynamic/structural information is passed thanks to the meshless method.

The static response, used to start a simulation from a steady state condition, is depicted in Fig. 13. It is obtained with a static aeroelastic tool consistent with the above employed hypotheses. It may be well noticed that the snap-divergence has now a more pronounced connotation.

In Figs. 13 and 14, the dynamic responses obtained starting from different velocities and applying the above described perturbation are given. It may be observed how, with this more realistic modeling, the flutter speed sensibly decreases if compared with the outcome of the previous analysis. In fact, even for structural damping ratio ζ different than zero and subcritical (in term of flutter) speeds, when the case was analyzed with the *Solver1*, an LCO was observed.

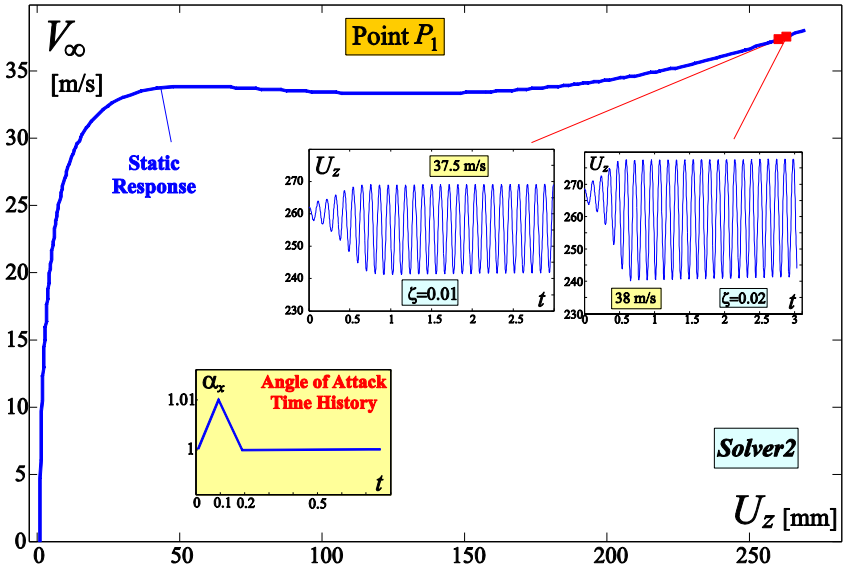

Fig. 13 *Solver2*. Aeroelastic dynamic response of *JW70* starting from steady states relative to different velocities when a vanishing perturbation of angle of attack of the onset flow is given. Different structural damping values are considered.

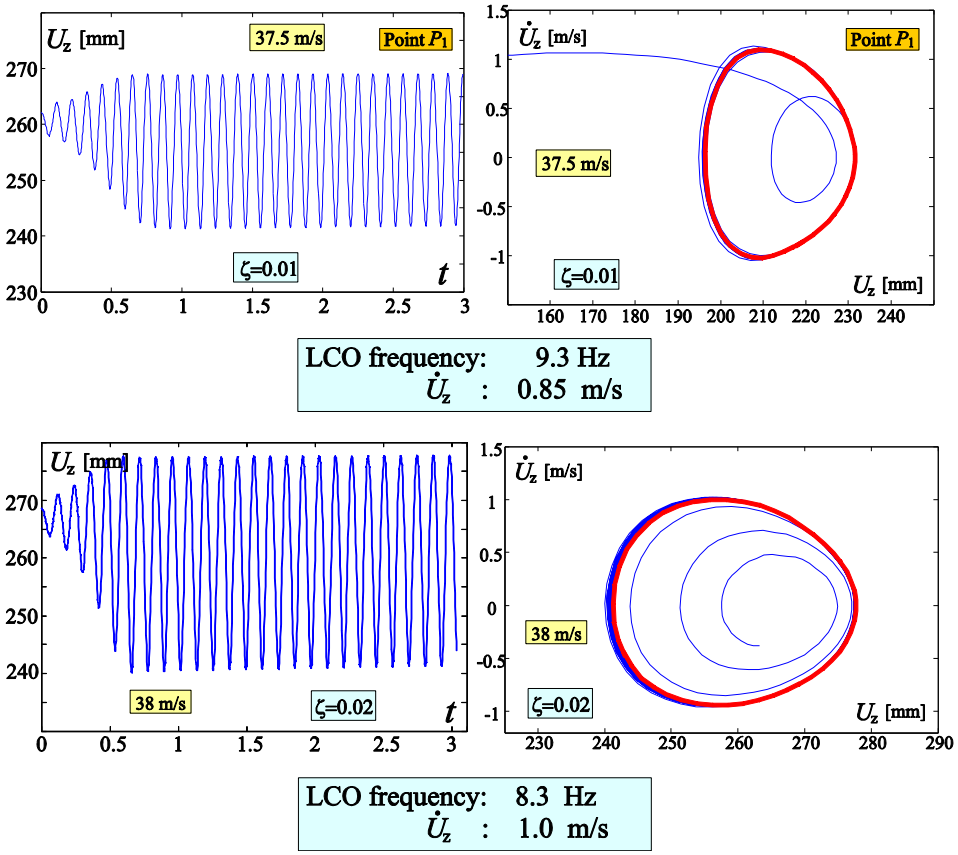

Fig. 14 Time response and phase-space trajectory for *JW70* configuration, for different flow speeds. *Solver2* is employed

7.1.3 Solver 3

The capability of free wake is considered in *Solver3*. Moreover, the vortex rings are now considered attached to the structure. Thus, differently than *Solver2*, there is a perfect consistency between the control point where boundary condition is applied and inducing singularities panels.

To consistently compare the results to the above presented ones, it is necessary to find a suitable steady state condition. There are two generic ways to achieve a steady state. One method is based on an iterative process starting from an initial first guess wake geometry, moving it accordingly with the induced velocity components parallel to a plane perpendicular to the freestream velocity (see Katz and Plotkin 2001). A further way to proceed is just to start from a rest condition and follow the transient until a steady state is reached.

Here, an approach similar to the second one is employed. In fact, an impulsive start is given to the configuration, and the angle of attack is slowly increased until it reaches the sought value (in Fig. 15 the time history of the angle of attack is depicted). When these simulations are carried out for larger speeds than the flutter one, then, obviously, a steady state is not observed.

Results are summarized in Fig. 15. The time histories suggest that the flutter speed lies in the $36 \div 38$ m/s range, probably closer to 38 m/s. In fact, the LCO observed at this speed has very limited amplitude, indicating that the state is one immediately following a Hopf's bifurcation.

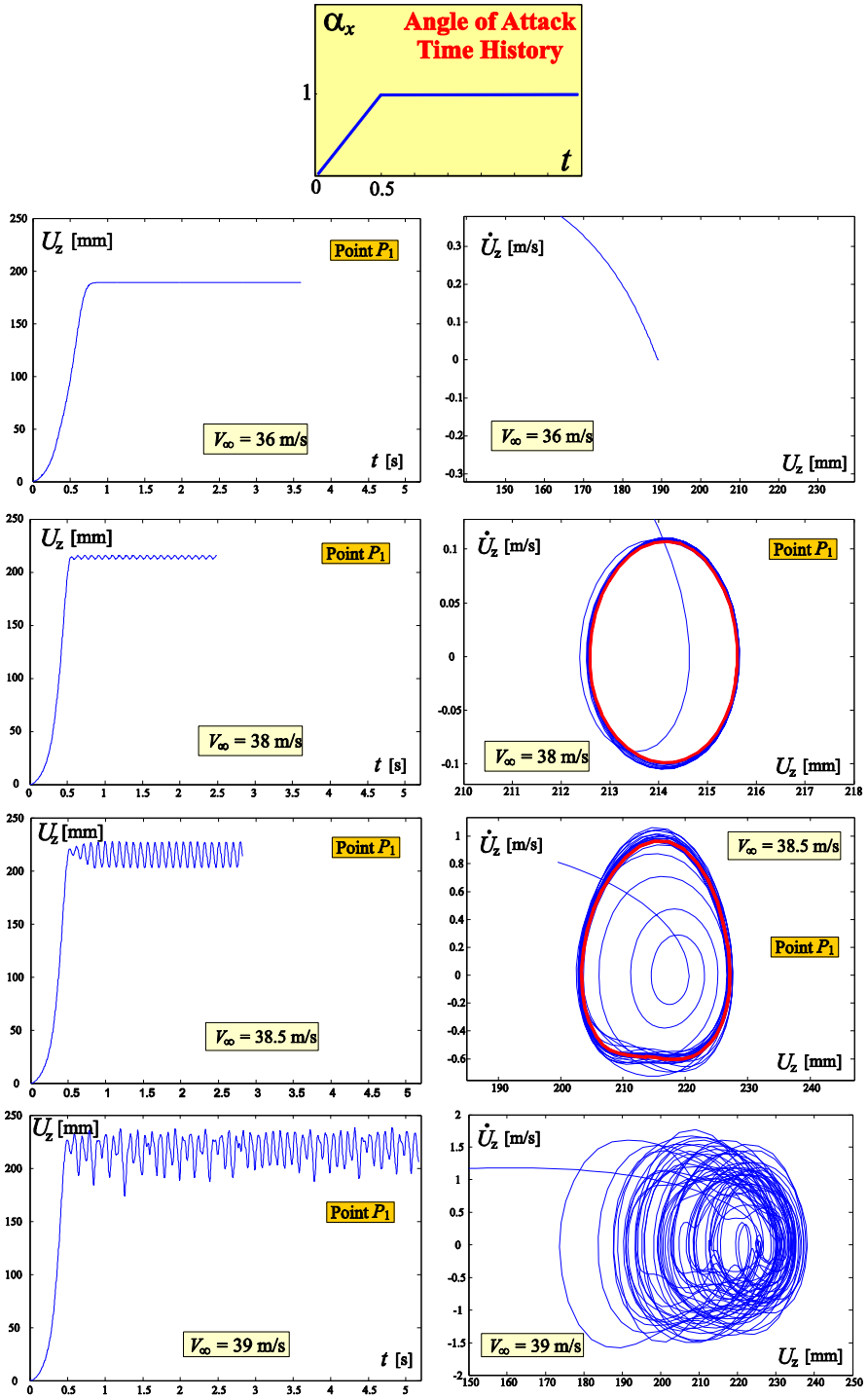

Fig. 15 Time response and phase-space trajectory for *JW70* configuration, for different flow speeds. *Solver3* is employed. The angle of attack is increased linearly from 0° to 1° in 0.5 seconds. No structural damping is considered. The *LCO* observed at a speed of $V_\infty = 38\ \mathrm{m/s}$ has a frequency of 10.8 Hz. The one at $V_\infty = 38.5\ \mathrm{m/s}$ has a frequency of 10.5 Hz

With a small increase in speed, the LCO has larger amplitude. With a further increment of speed, the response does not seem to have any periodicity, suggesting a transition toward chaos. An in-depth analysis is needed to affirm and demonstrate the above possible chaotic behavior.

It is very interesting to notice how a relatively small variation in speed (see Fig. 15) significantly changes the nature of response.

7.1.4 Effects of solver's choice and structural damping on flutter speed

In Fig. 16 it is plotted the flutter speed, as evaluated with the different solvers, with respect to the structural damping ratio. The critical speeds evaluated with the time-domain solvers are obtained by considering the two successive speeds for which the response was showing and was not showing an LCO. In the graph, the DLM overestimates the flutter speed in respect with all other methods. In particular, *Solver1* uses the same aerodynamic and load transferring of the DLM one, thus, to prove that this difference is not an artifact of numerics, the number of natural modes, aerodynamic panels and structural elements have been verified to be sufficient to give convergent results (the details are here omitted for brevity).

Solver2 gives lower flutter speeds. Applying the lift in the appropriate direction and consider the real normal in the application of the boundary condition exacerbates the bending actions. However, in general, even if in agreement with intuition, the above argument may not hold. For example, it will be shown for the *PrP40* layout that this is not the case.

With *Solver3*, the singularities are bound to the structure, and the wake is free to deform and evolve. Especially these last features have a relevant role in increasing the critical speed.
All the solvers show a similar trend of the flutter speed with the structural damping.

7.2 Limit cycle oscillation for PrP40

This section retraces the logic of the previous part. However, the configuration under examination is now the *PrP40*. See Fig. 6 for details about the geometry. For this specific test case, the thickness of the wings is set to $t = 1\,\mathrm{mm}$. The modality of application of the perturbation strictly follows what done in the previous section.

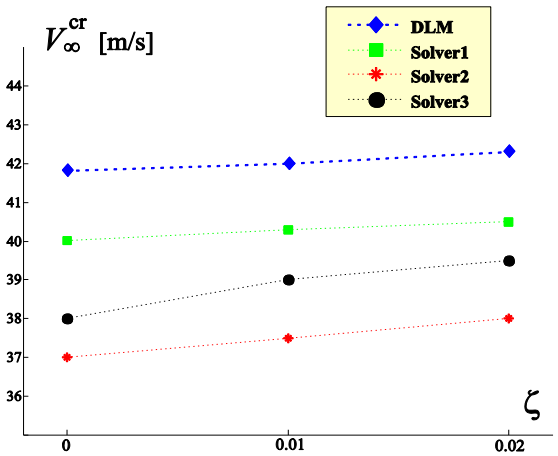

Fig. 16 Flutter speeds for *JW70* configuration, evaluated with the different solvers and for different structural damping ratio values

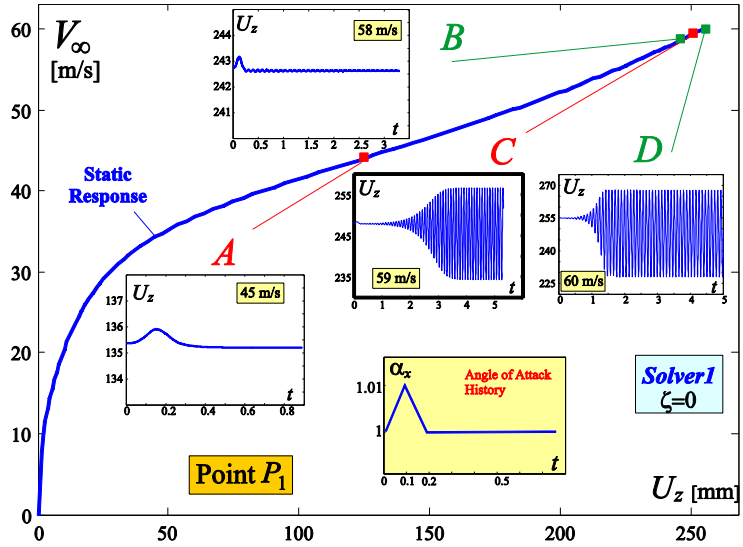

Fig. 17 *Solver1*. Aeroelastic dynamic response of *PrP40* starting from steady states relative to different velocities when a vanishing perturbation in angle of attack of the onset flow is given

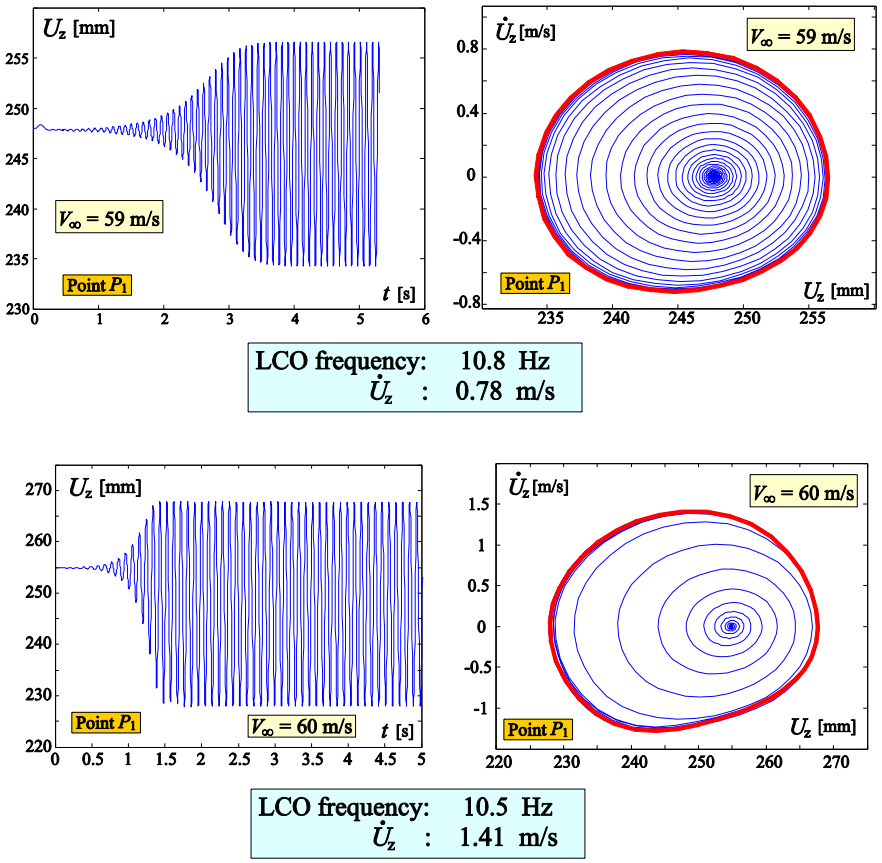

Fig. 18 Time response and phase-space trajectory for *PrP40* configuration, for different flow speeds. *Solver1* is employed. No structural damping is considered

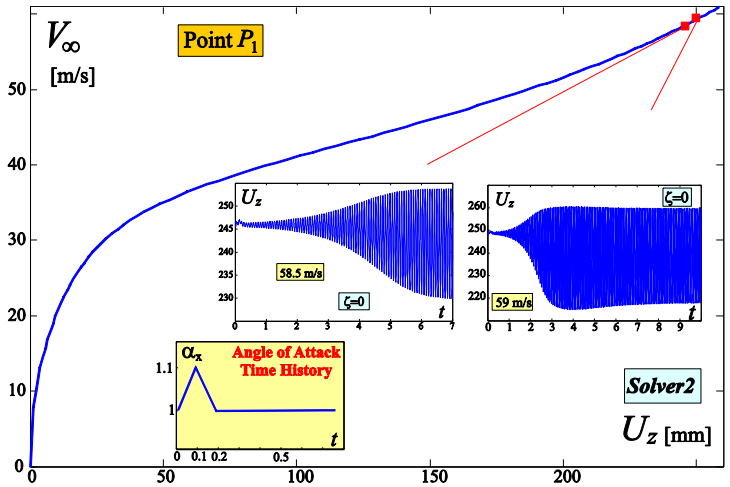

Fig. 19 *Solver2*. Aeroelastic dynamic response of *PrP40* starting from steady states relative to different velocities when a vanishing perturbation in angle of attack of the onset flow is given

7.2.1 Solver 1

Fig. 17 shows both the aeroelastic static response, and the time evolution of the *PrP40* configuration starting from an equilibrium state depicted in the graph and experiencing a vanishing perturbation. As for the *JW70* case, this disturbance consists in a linear increase in the angle of attack (formed by the onset flow direction and the *x*-axis), followed by a symmetric decrease to the unperturbed value (which is 1°). For all cases the structural damping is set to zero. Both configurations relative to subcritical and supercritical speeds are chosen.

The outcome of the simulations suggests that the flutter speed is in the $58 \div 59\ \mathrm{m/s}$ range. Observing the response for speed larger than the flutter's one, it may be noticed how, differently than the *JW70* case, the response is not settling to his final LCO with the typical pattern observed before, in which the oscillating motion was very slowly cutting its amplitude and shifting its mean value before reaching the asymptotic behavior.

On the contrary, after a very brief peak, the response immediately sets to the asymptotic mean value, and the amplitude of the oscillations rapidly reaches the regime one. This could be observed with the aid of Fig. 18.

Repeating the simulation with a value of the damping ratio $\zeta = 0.03$ the critical speed increases, however, the time response reminds the ones of the undamped system. Thus, these cases are not shown here for brevity.

7.2.2 Solver 2

The static aeroelastic response is first obtained in a way consistent with the hypothesis of the aerodynamic solver. Then, picking a speed, the initial configuration is automatically chosen, the perturbation is applied and the response is studied. Results are shown in Fig. 19, whereas the LCOs in the phase-space diagram are given in Fig. 20.

An interesting direct comparison of LCO's properties at a fixed speed ($59\ \mathrm{m/s}$), obtained by two different solvers is shown in Fig. 21. Exploiting the geometrical follower nature of the aerodynamic forces (taken into account with *Solver2*) has an important effect on the amplitude of the LCO, and also on the frequency: both of them increase by a considerable extent. Although it is

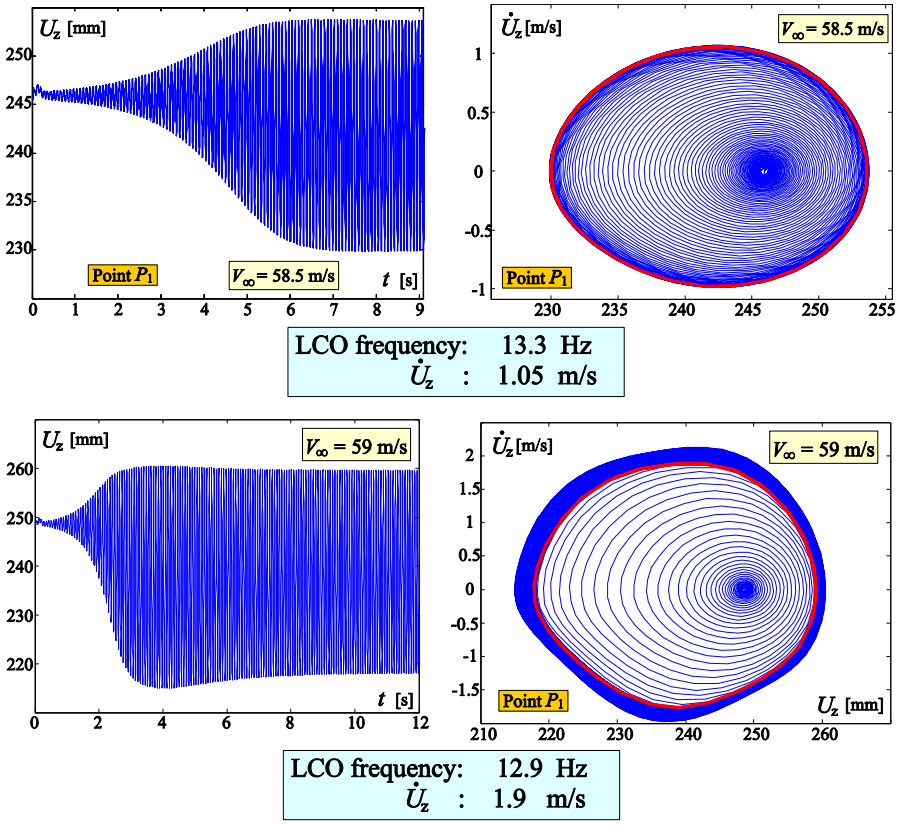

Fig. 20 Time response and phase-space trajectory for *PrP40* configuration, for different flow speeds. *Solver2* is employed. No structural damping is considered

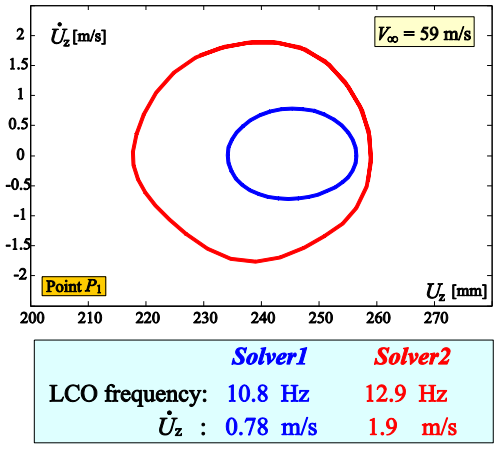

Fig. 21 LCOs of *PrP40* at a speed of V_∞ = 59 m/s as predicted by *Solver1* and *Solver2*.

always difficult to rely on intuition when studying nonlinear dynamic aeroelastic phenomena, the increase in amplitude "is expected" in the sense that a follower force tends to exacerbate the deformation.

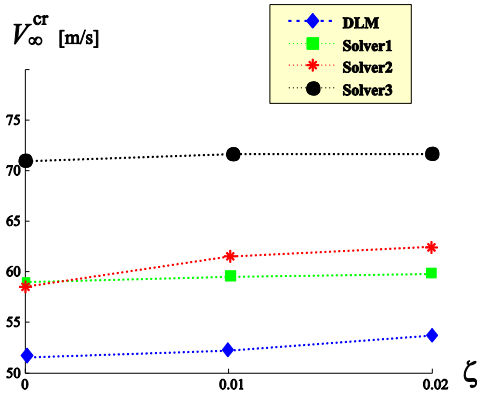

Fig. 22 Flutter speeds for *PrP40* configuration, evaluated with the different solvers and for different structural damping ratio values

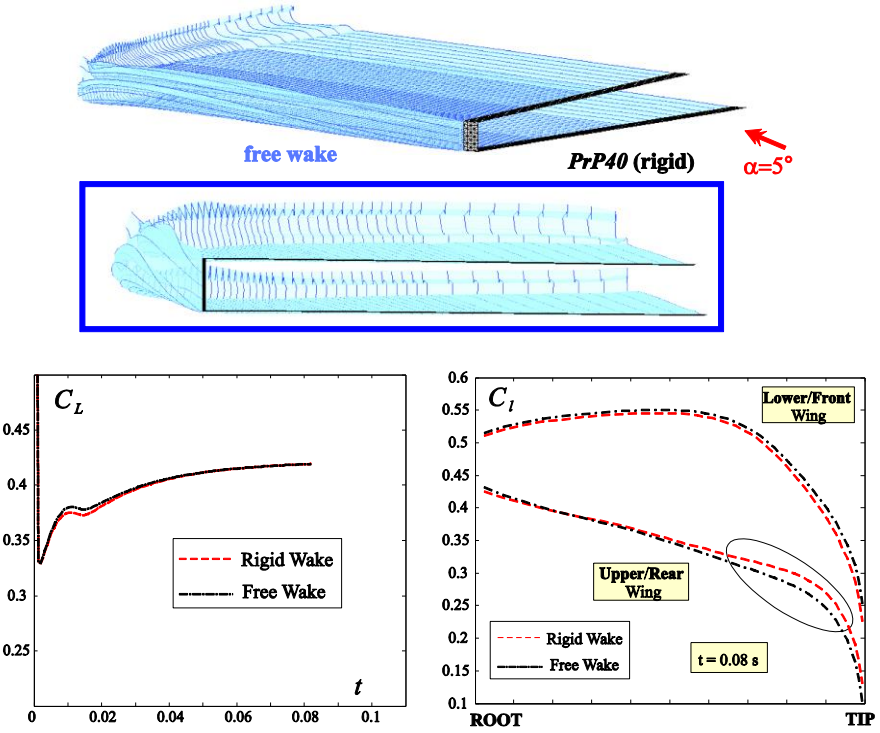

Fig. 23 Wake models and their effects on the lift coefficients of the PrP40's wings

7.2.3 Solver 3

Time responses and phase-spaces of the limit cycle oscillations found by means of the *Solver3* are not reported. However, the performances of this tool in predicting flutter speed are analyzed in the next section.

7.2.4 Effects of solver's choice and structural damping on flutter speed

Fig. 22 presents the flutter speed, evaluated with the different solvers, as a function of the

structural damping ratio. Considering the undamped case, the DLM solver found a flutter speed of approximately $51.5\,\mathrm{m/s}$, whereas, *Solver1* predicts a critical speed of $58.5\,\mathrm{m/s}$. The relative error is in the order of 12%, definitely larger than the discrepancy observed for the *JW70* case. Further analyses are needed to explain this difference. A further comment is that, differently than previous case, now the DLM predicts the lowest speed, giving thus a conservative estimation of the flutter speed.

Another difference from the *JW*70 case is the higher flutter speeds predicted by *Solver2* when compared to *Solver1*, for nonzero damping ratios.

However, the most relevant observation is the discrepancy of *Solver3* with all other solvers. Here, an explanation is tempted based on physical arguments. Comparing *Solver3* with *Solver2* the most significant source of differences is the treatment of the wake. To isolate this effect, a pure aerodynamic case is introduced.

An impulsive start of an undeformable *PrP40*, immersed in a flow with an angle of attack of 5° is now considered. Both a rigid wake and a flexible (free) wake model are used. The lift coefficient evolution in time is depicted in Fig. 23.

In the immediate transient there is a small difference between the lift coefficients. This difference vanishes when evolving in time. If, for a time in which the global lift coefficients are identical, the lift distribution along the wingspan is compared, effects of the different modeling of the wake could be better appreciated. With the free wake there is a decrease, especially concentrated on the outer part of the upper wing, of the lift; on the other hand on the front wing there is an almost uniformly distributed increase.

A similar aerodynamic study was repeated for an unstaggered PrandtlPlane-like configuration: it was deduced that the large load redistribution due to wake deformation was not just strictly connected with the stagger of the *PrP40* configuration. Thus, it is expected that also the other joined-wing layouts experience considerable load redistribution when a free-wake model is adopted. The question has still to be answered regarding why the PrandtlPlane-like configuration is much more sensitive to the wake modeling.

The following speculative explanation could be attempted. It may be noticed that in this configuration both of the wings extend spanwise to the same amount and the redistribution of loads on the wing-tip area has large bending moment effects due to the large moment arm with respect to the wing root. Thus, it seems reasonable to link these actions to a consistently different aeroelastic response. However, as said, this has to be demonstrated, especially considering that this redistribution is of course particular of the specific case under examination (undeformed wings), and thus it is not immediate to extend these results to the real deformed case.

A further note about the redistribution is that it affects the induced drag of the configuration. This was already shown in reference (Bernardini 1999), in which a free-wake modeling was predicting a lower induced drag whereas the lift coefficient was not experiencing differences. It is then suggested that, application of classic formulae (Prandtl 1924, Frediani and Montanari 2009, Demasi *et al.* 2014) for a first evaluation of the induced drag may be slightly penalizing.

7.3 Sensorcraft

Now the *Sensorcraft* configuration is considered. The undisturbed flow forms with the x-axis an angle of $3°$, and this enables to track an aeroelastic static response as shown in Fig. 24. The dynamic response is studied applying a vanishing perturbation in angle of attack, as described for the previous cases.

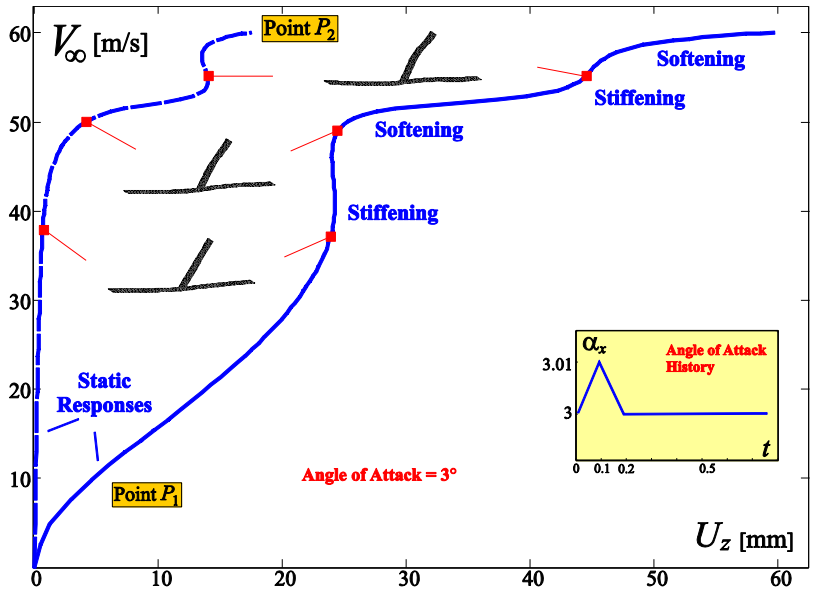

Fig. 24 Aeroelastic static response of *Sensorcraft*. Vertical displacements of points P_1 and P_2 are taken into consideration (see Fig. 7). Angle of attack is 3°. The vanishing perturbation that is applied to track the dynamic response is also represented

7.3.1 Solver 1

Solver1 is here used to track the response. However, before further proceeding, it is interesting to comment the aeroelastic static response of this configuration, as shown in Fig. 24. It features the vertical displacement of both point P_1, lying on the wing tip, and P_2, at the mid-span (as depicted in Fig. 7). The extreme nonlinear response presents a sequence of softening and stiffening. In the first stiffening region (for wing's tip), the deformation of the upper wing produces a bending moment transmitted directly to the lower wing, such that the tip of the wing does not experience any vertical displacement for a wide range of speeds.

Dynamic responses are presented in Fig. 25 for different speeds. Focus is first on the LCO at $V_\infty = 52.5$ m/s. Considering the mid-span point P_2, the trajectory described by this point when a limit cycle oscillation is established is the usual wave-like response. However, this does not hold for wing tip P_1. In fact, considering a period, during the ascending part the motion is temporary reversed and some higher frequency oscillations of smaller amplitude establish before continuing again the ascending motion. The descending motion does not show such a pattern. This response has been observed also when structural damping was considered (not shown here) suggesting thus, that this phenomenon is not an artifact of numerics but rather real expression of the physics.

If the speed is slightly increased to $V_\infty = 53.5$ m/s the same pattern is observed, however now the oscillation in the ascending motion increases its amplitude. It is natural then to repeat this process for higher speeds and observe what happens. A speed of $V_\infty = 59$ m/s is considered, and the response is depicted in Fig. 26. An aeroelastic stable fixed point seems to exist even if the speed is larger than the previous cases (having LCOs). This result is unexpected and underlines, once again, the difficulties inherent to the design of such a configuration. With the aid of Fig. 27 this property is better shown: starting from a stable situation, the speed is slowly decreased until a

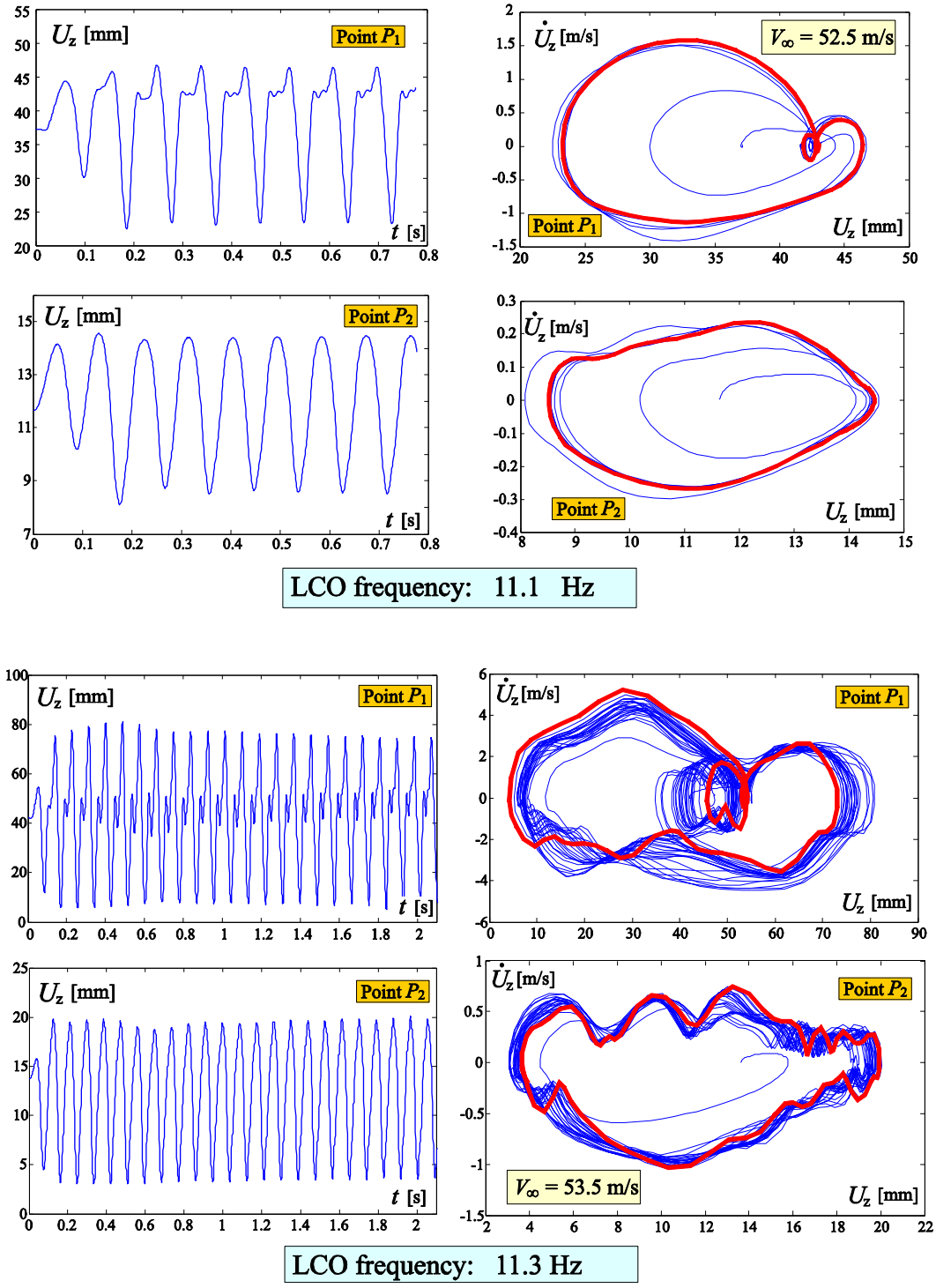

Fig. 25 Time response and phase-space trajectory for *Sensorcraft* configuration, for different flow speeds. *Solver1* is employed. No structural damping is considered. Vertical displacements of both points P_1 and P_2 are considered (see Fig. 7)

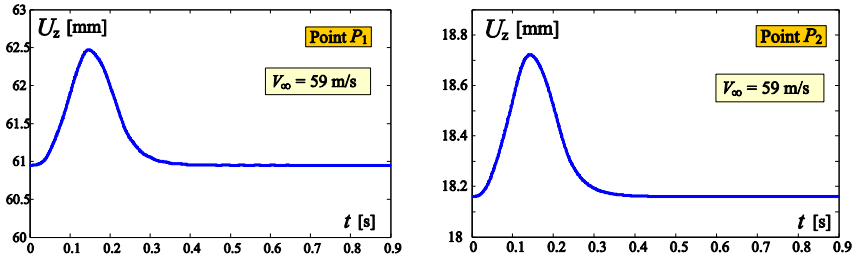

Fig. 26 Time response for *Sensorcraft* configuration, for V_∞= 59 m/s. *Solver1* is employed. No structural damping is considered. Vertical displacements of both points P_1 and P_2 are tracked (see Fig. 7)

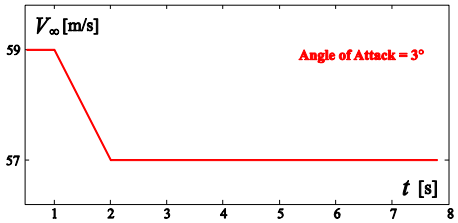

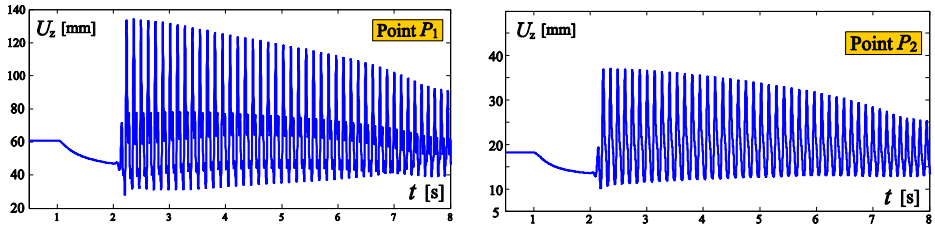

Fig. 27 Time response for *Sensorcraft* configuration, when the speed is decreased from $V_\infty = 59$ m/s to $V_\infty = 57$ m/s, and the angle of attack is maintained to 3°. *Solver1* is employed. No structural damping is considered. Vertical displacements of both points P_1 and P_2 are tracked (see Fig. 7)

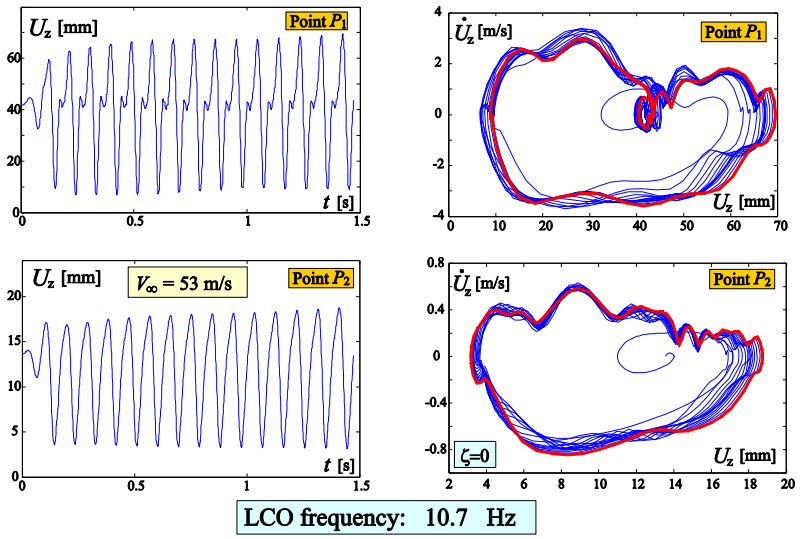

Fig. 28 Time response and phase-space trajectory for *Sensorcraft* configuration at a speed $V_\infty = 53$ m/s. *Solver2* is employed. Vertical displacements of both points P_1 and P_2 are tracked (see Fig. 7)

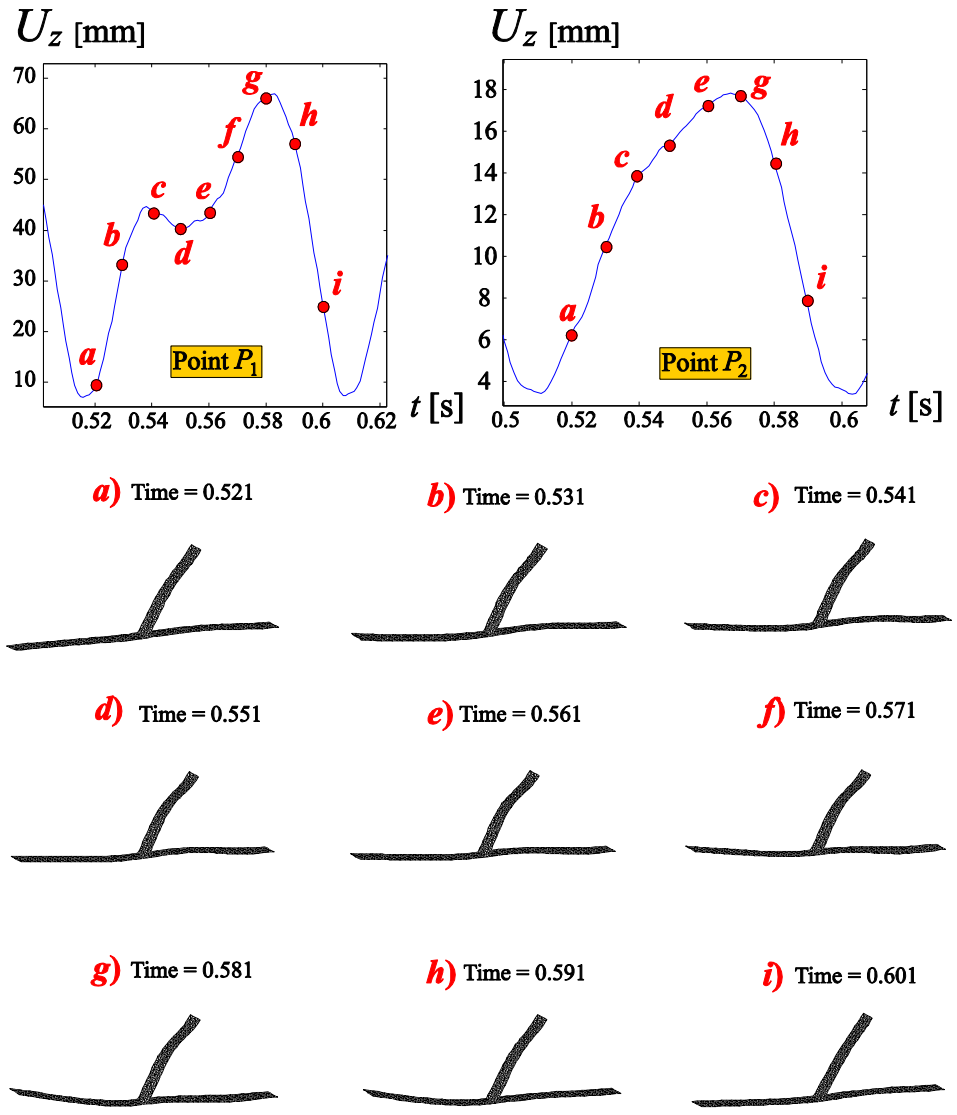

Fig. 29 Sequence of snapshots of the deformed configuration during one period (LCO). *Solver2* is employed and $V_\infty = 53$ m/s. Points *c*, *d* and *e* represent the small oscillation in the ascending motion

critical condition is reached. It can be assessed how, for $V_\infty = 57$ m/s the response immediately loses its stability (in the static sense) and an LCO is developed after the transient.

7.3.2 Solver 2

Use of *Solver2* does not seem to give large differences from what previously observed. What can be noticed is a small decrease of the frequency, as shown in Fig. 28.

The same oscillating pattern during the ascending motion is identified. In order to better visualize this phenomenon, it is interesting to plot the *snapshots* of the configuration during a period, Fig. 29. As it can be easily verified, the states *c*, *d* and *e* describe the small oscillation

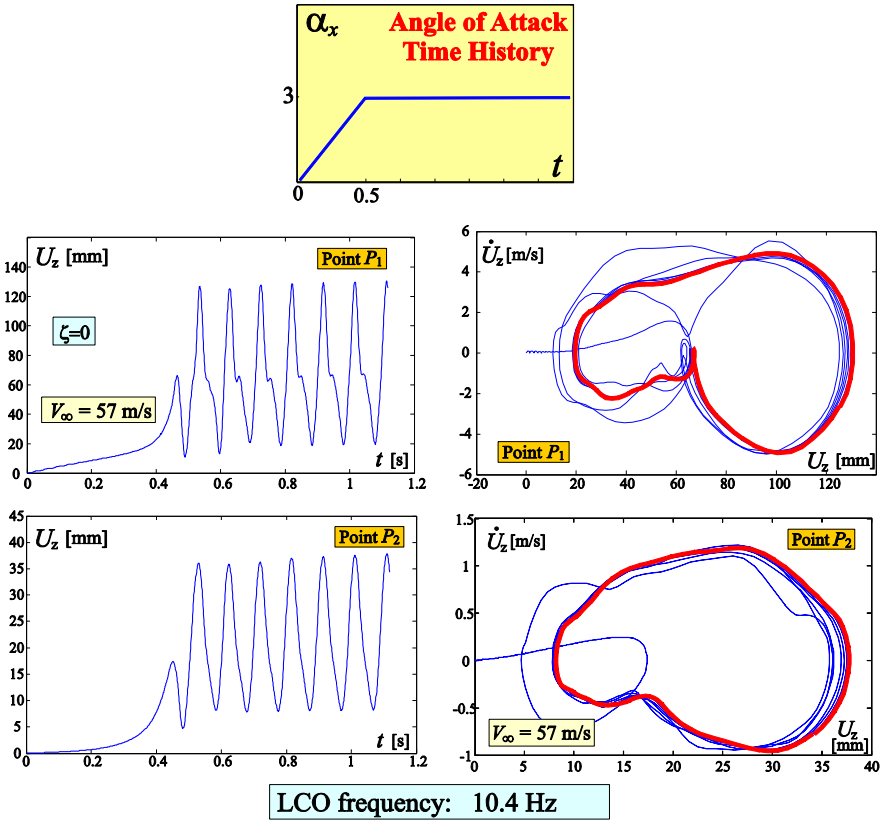

Fig. 30 Time response and phase-space trajectory for *Sensorcraft* configuration, for $V_\infty = 57$ m/s. *Solver3* is employed. Vertical displacements of both points P_1 and P_2 are tracked (see Fig. 7)

during the ascending motion. Focusing then on the upper wing, it can be observed a unique smooth wave-like pattern identified by a compression and an extension, whereas for the outer portion of the wing this does not hold. It is not trivial to understand why the portions of the wing system have different dynamics, since different sources of difficulties are present: nonlinear structure, coupled aerodynamic structural and inertial effects, and also overconstrained nature of the system. As it will be shown in the next section, adding a further source of nonlinearity (wake roll up) also influences the above mentioned pattern.

7.3.3 Solver 3

Results obtained with *Solver3* are presented in Fig. 30. The speed is selected so that it is possible to observe the small oscillation pattern of the tip of the wing (point P_1). The angle of attack is increased until the value of 3° is obtained. It is interesting to notice that the high frequency oscillation pattern earlier described is now appearing in the descending portion of the LCO. To visualize this pattern, *snapshots* of the configuration during a period are presented in Fig. 31.

States *f*, *g* and *h* describe the small oscillation during the descending motion. Even if the mid-span point P_2 is monotonically descending in this window of time, the outer portion of the wing inverts its motion, bending upward before restarting its descend.

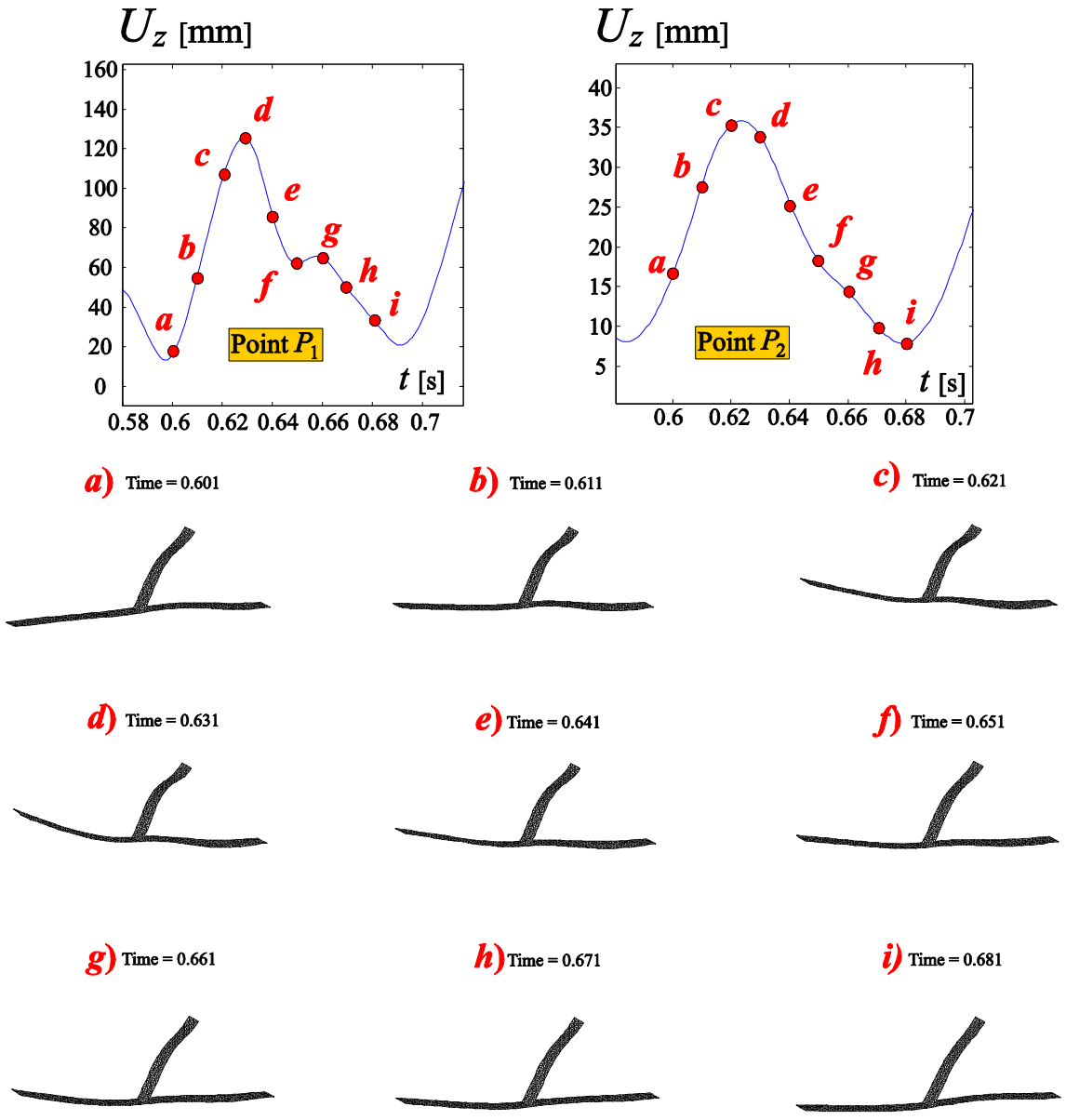

Fig. 31 Sequence of snapshots of the deformed configuration during one period (LCO). *Solver3* is employed and $V_\infty = 57$ m/s. Points *f*, *g* and *h* represent the small oscillation in the descending motion

7.3.4 Effects of solver's choice and structural damping on flutter speed

Fig. 32 shows the flutter speed, evaluated with different solvers, as a function of the structural damping ratio. The predictions are now much closer, and the differences are negligible. This is related both to the particular layout and to the smaller involved deformations, which do not enhance the modeling differences of the solvers.

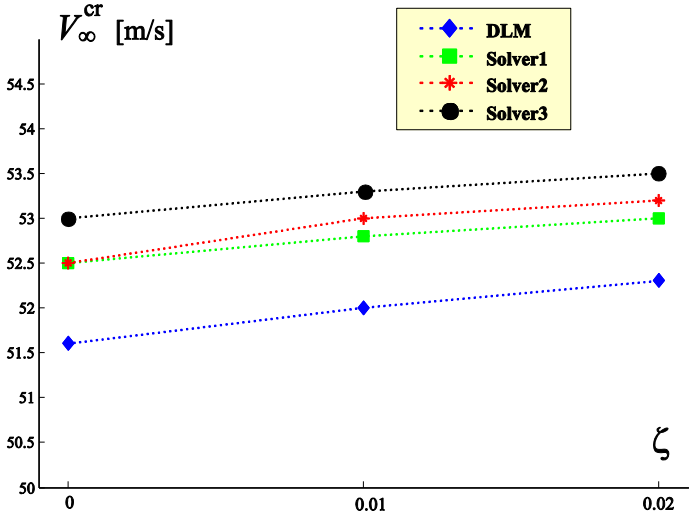

Fig. 32 Flutter speeds for *Sensorcraft* configuration, evaluated with the different solvers and for different structural damping ratio values

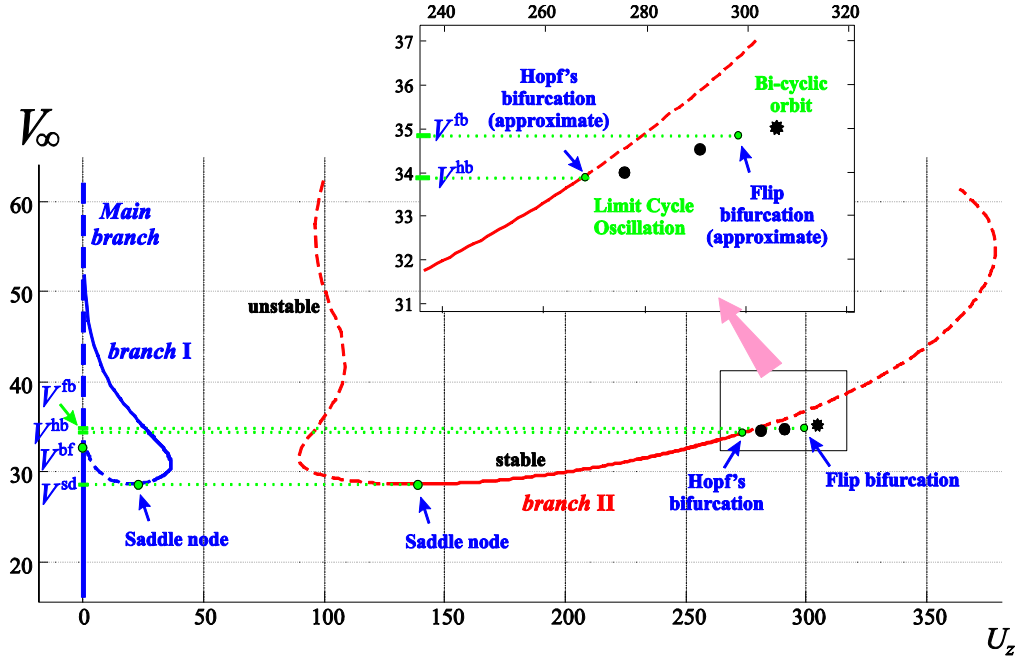

Fig. 33 Bifurcation diagram for the testcase. *Solver1* is employed. Solid (dashed) lines represent stable (unstable) fixed points, full circles stand for stable limit cycle oscillations (the largest value is depicted) and the full complex stars stand for stable bi-cyclic periodic closed orbit (largest value is depicted in the graph)

8. Joined wings: a dynamical system perspective

This section shows the complicate picture of joined-wing responses described from a dynamical system perspective. Different kinds of bifurcations are detected leading to a variegated

stability diagram.

The *PrP40* layout is considered (see Fig. 6), and the thickness is now selected to be 0.6 mm. The freestream velocity is along the x axis (zero angle of attack). *Solver1* is used to study the dynamic response. As it will be clear in the following, aeroelastic static tools with continuation capabilities (arc-length methods) are also used.

Being the angle of attack zero, there are no aerodynamic forces in the undeformed (basic) configuration. Thus, it is an equilibrium (fixed point) condition for all velocities. With reference to the bifurcation diagram of Fig. 33, in which the vertical displacement of the tip of the lower wing (point P_1 in Fig. 6) has been chosen as representative displacement variable and the parameter is the flow speed, these fixed points lie on the ordinate.

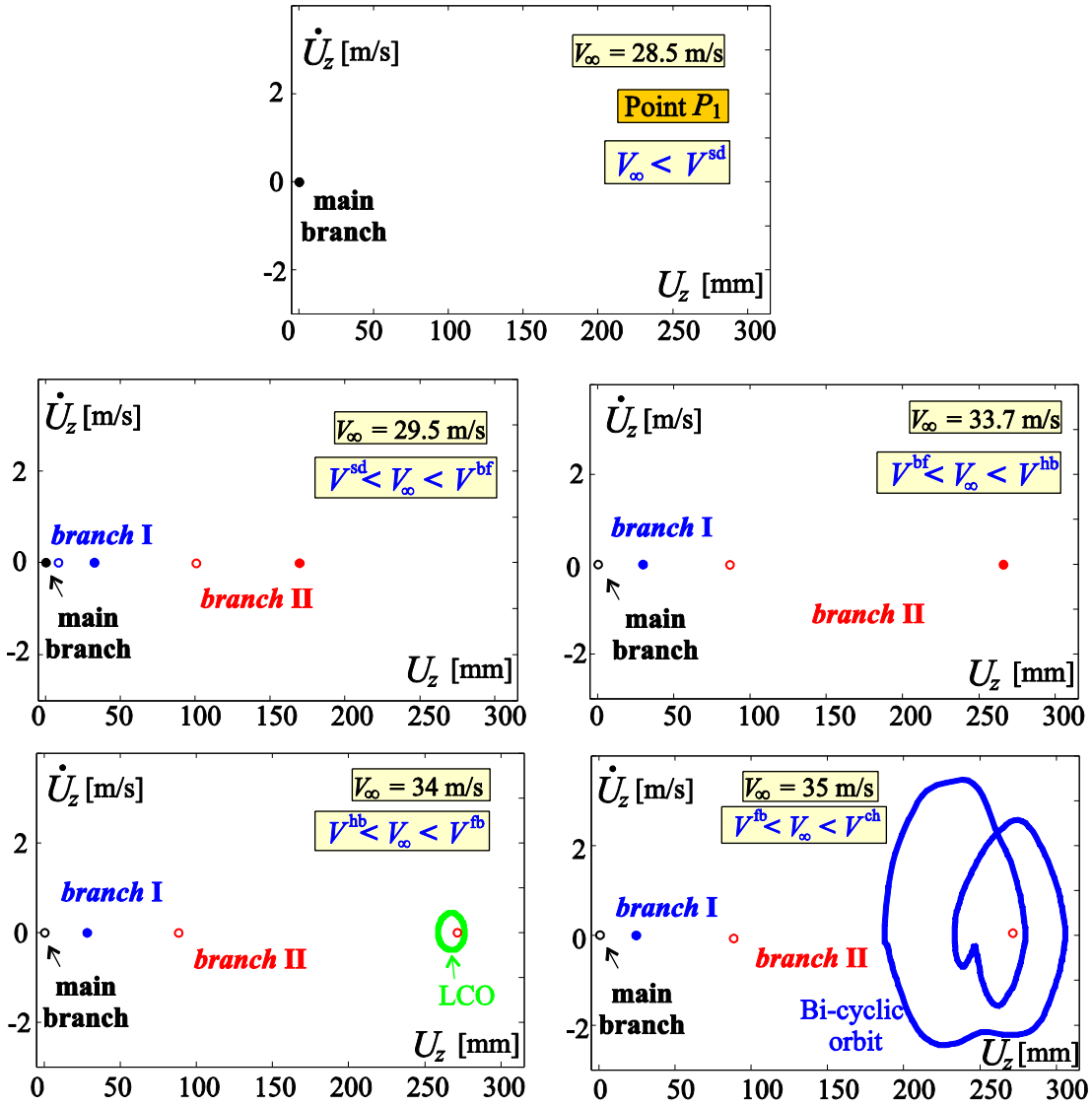

Fig. 34 Phase-space for different speeds

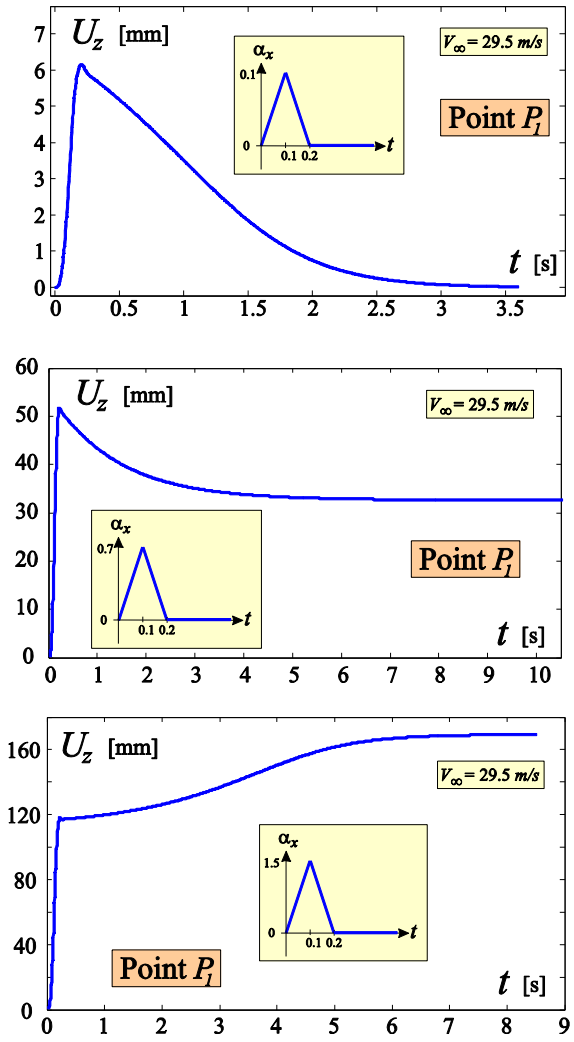

Fig. 35 Tri-stability region, at $V_\infty = 29.5$ m/s. Starting from the initial undeformed configuration different vanishing perturbations of angle attack are given, and the response is tracked

If, starting from zero, speed is increased, V^{sd} is reached. This speed is associated with saddle node bifurcations taking place on branches far from the fundamental one. What occurs is the inception of two fixed node points on each of the non-fundamental branches. As a consequence, if the speed falls between V^{sd} and V^{bf}, there are *five possible equilibrium configurations*, and three of them are *stable*, see Fig. 33. Thus, a so called *tri-stability* situation is in place. With the aid of Fig. 34, a speed in this range has been chosen, i.e., $V_\infty = 29.5$ m/s, and the equilibrium points are represented with a small circle, full (empty) if they are stable (unstable).

Consequences of multi-stability have already been explored and discussed for joined-wing layouts in Cavallaro *et al.* (2013a), where branch-jumping phenomena were discussed. In Fig. 35 it is shown how, giving different vanishing perturbations of angle of attack, after the transient the configuration could settle to the three different equilibrium states on the branches.

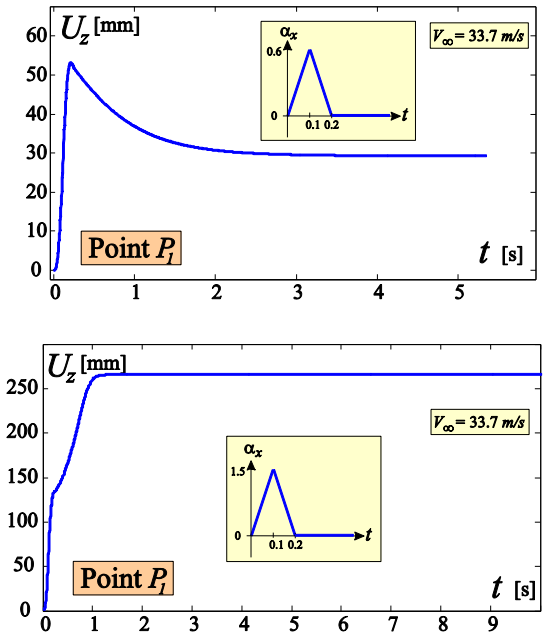

Fig. 36 Bi-stability region, at $V_\infty = 33.7$ m/s. Starting from the initial undeformed configuration different, vanishing perturbations of angle attack are given, and the response is tracked. The systems could settle down to both static equilibrium states on branches I and II

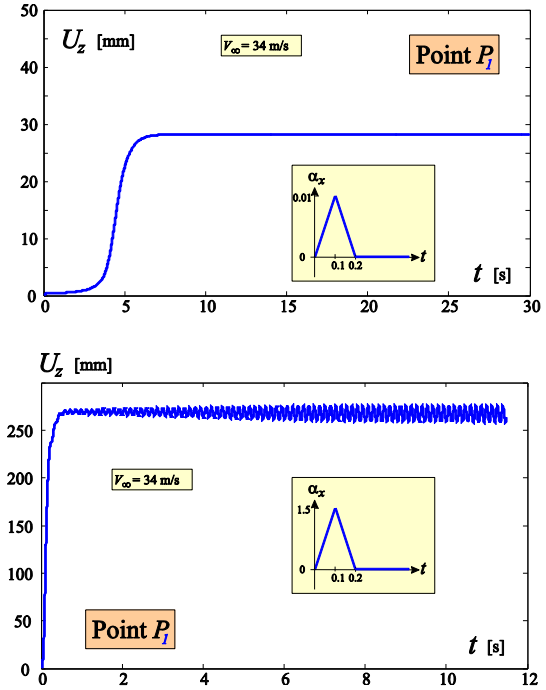

Fig. 37 Bi-stability region. Starting from the initial undeformed configuration different vanishing perturbations in angle attack are given, and the response is tracked. Either the static solution on branch I or the limit cycle oscillation is approached after a transient

When speed approaches V^{bf}, there is a bifurcation that leads to change of stability of the main branch: the undeformed configuration loses its stability. What happens in the negative part of U_z is here not studied, thus, any fixed point that may exist in that part of the plane has not been taken into consideration. The typical phase-space diagram for $V_\infty = 33.7\ \mathrm{m/s}$, which is in the range $V^{\mathrm{bf}} \div V^{\mathrm{hb}}$, is depicted in Fig. 34. There is a bi-stability, being the stable states on the branches I and II. There are also two unstable poles, the first being on the undeformed configuration and the other one on the branch II. Responses showing this behavior are represented in Fig. 36.

Increasing the speed, it is finally found a Hopf's bifurcation, V^{hb}. This bifurcation occurs for the branch II only. The fixed static solution becomes unstable, and, on the contrary, a stable limit cycle oscillation is developed. The properties of the points on the other branches do not change. Thus, as it is shown for a speed of $V_\infty = 34\ \mathrm{m/s}$, which is in the $V^{\mathrm{hb}} \div V^{\mathrm{fb}}$ range, perturbations lead to responses shown in Fig. 37.

The largest bifurcation speed found in this analysis is V^{fb}, for which a flip bifurcation (also called period doubling) occurs. For speeds slightly larger than V^{fb}, then, considering that the only stable fixed point lies on the branch I, there is still a bi-stability. This is shown also in Fig. 38.

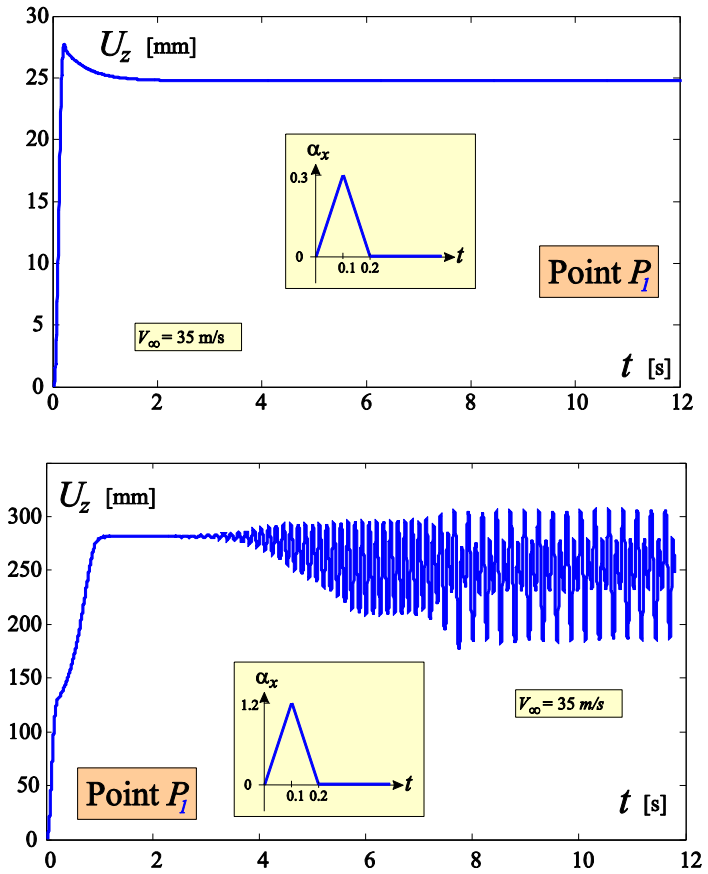

Fig. 38 Bi-stability region. Starting from the initial undeformed configuration different vanishing perturbations of angle attack are given, and the response is tracked. Either the static solution on branch I or the bi-cyclical closed orbit is approached after a transient.

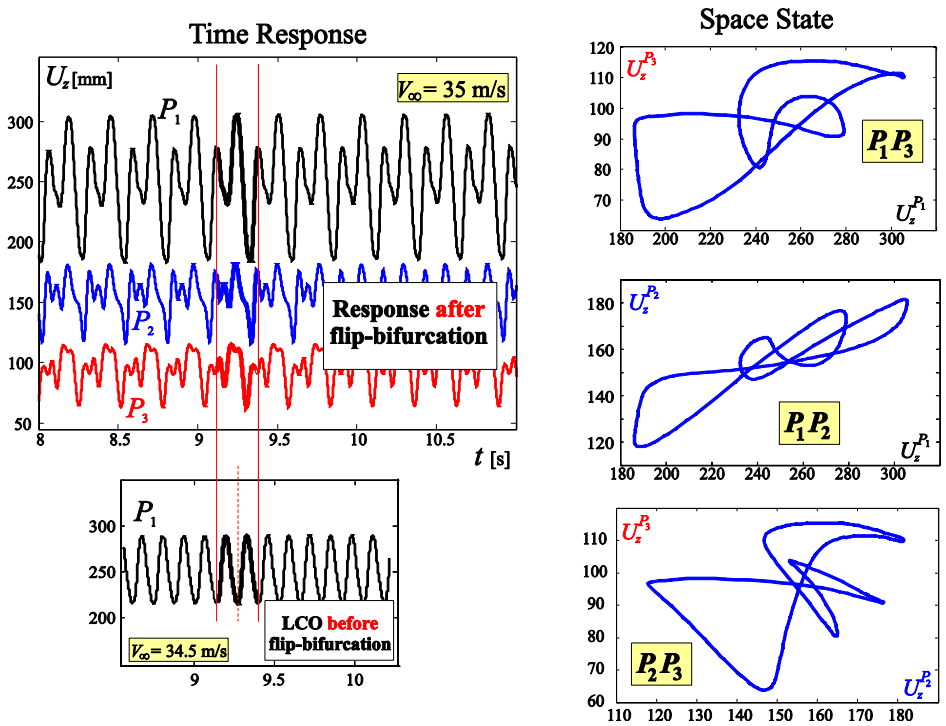

Fig. 39 Closed orbit for higher than flip bifurcation speeds. Time response for points P_1, P_2, P_3, and phase-spaces for their combinations. The time responses are also compared to a subcritical one to assess the doubling of the period

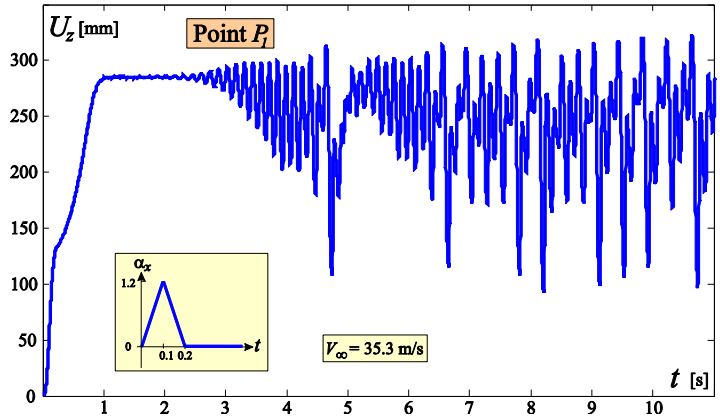

Fig. 40 Time response for $V_\infty = 35.3$ m/s when a vanishing perturbation in angle attack is given: the response does not show any periodicity

It is important to notice that, to mathematical assess a flip-bifurcation occurrence the eigenvalues of the so called *Monodromy Matrix*, known also as Floquet characteristic multipliers, (Seydel 2009, Quaranta *et al.* 2003) have to be studied. However, this analysis is not trivial when relatively large (in terms of number of DOFs) systems are considered. Thus, this was not pursued in this study. On the contrary, period doubling was assessed noticing that, immediately after the

bifurcation point, the period of the closed orbit was doubling compared to the one of the limit cycle oscillation established at a speed lower than the period doubling one. Fig. 39 clearly shows the doubling of the period.

The closer orbit described after period doubling occurrence is here assessed to as bi-cyclic periodic orbit. It is presented more in detail in Fig. 39. The time responses as well as the phase-spaces are plotted considering now three degrees of freedom. Other than the point P_1, now also vertical displacements of points P_2 and P_3 (see Fig. 6 for their position).

When speed is further increased, the response associated with the branch detached from the period doubling bifurcation seems to have a chaotic response, as shown in Fig. 40. In depth analyses are needed to confirm transition to chaos. The branch I stable fixed point is still present (Fig. 33).

9. Conclusions

Dynamic aeroelastic phenomena of Joined Wings with the inclusion of geometrical nonlinearities have been here presented. Investigating the behavior of different typical layouts, this effort was directed towards different perspectives.

First, a dynamic characterization of the *snap-divergence* concept was given. In fact, its occurrence was first found and examined by means of aeroelastic static analyses in previous publications (Demasi *et al.* 2013b). The question was then to assess its existence and the real dynamic behavior of the system. Results showed that the static predictions were correct, and the characteristic *snap* was observed.

Second, flutter analyses carried out with a linear frequency-domain tool were compared to nonlinear ones, obtained as a sequence of successive linearizations performed about deformed configurations. It was found that the linear tools were giving nonconservative predictions, supporting a trend shown in previous literature studies (Demasi *et al.* 2013a, Demasi *et al.* 2013b) carried out considering mechanical instability and aeroelastic divergence.

Third, the impact of different modeling of the aeroelastic problem (positioning of the aerodynamic singularities, boundary condition enforcement, interface method or wake description) on flutter speed was assessed for time-domain solvers. Comparisons with the above frequency-domain capability were also given. It was shown that, free-wake modeling was increasing flutter speed (at least for the configurations under examination), and this was put in relation with the particular architecture of the layout.

Fourth, aeroelastic dynamic postcritical regime was explored. Limit cycle oscillations were found. For some combinations of solvers and configurations the transient to the LCO showed unusual trends: phase-space transient trajectories did not resemble the final periodic orbits and the transients were relatively long. It was however difficult to give any further physical interpretation without having the support of experimental data. Moreover, for the SensorCraft-like configuration, at certain speeds, the limit cycle oscillation was showing, within a period, different patterns between the outer and inner parts of the wing system.

Fifth, the joined-wing behavior was studied in more depth on a dynamical system perspective. Bi-stability and tri-stability were observed, in analogy with what discovered in (Cavallaro *et al.* 2013a). For a certain speed, one branch was experiencing a Hopf's bifurcation (flutter), followed by a flip bifurcation (or period doubling). These are common symptoms suggesting a transition to chaos might be in place.

Acknowledgments

The authors acknowledge the support by San Diego State University (College of Engineering). They also like to warmly thank Professor Antonio Palacios of the Department of Mathematics of San Diego State University for his precious suggestions about nonlinear dynamics.

References

Attar, P.J., Dowell, E.H. and White, J. (2004), "Modeling the LCO of a delta wing using a high fidelity structural model", **3**, 1986-2000.

Attar, P. and Gordnier, R. (2006), "Aeroelastic prediction of the limit cycle oscillations of a cropped delta wing", *J. Fluid. Struct.*, **22**(1), 45-58.

Bernardini, G. (1999), "Problematiche aerodinamiche relative alla progettazione di configurazioni innovative", Ph.D. Thesis, Politecnico di Milano.

Bhasin, S., Chen, P., Wan, Z. and Demasi, L. (2012), "Dynamic nonlinear aeroelastic analysis of the joined wing configuration", *Proceedings of the 53rd AIAA/ASME/ASCE/AHS/ASC Structures, Structural Dynamics, and Materials Conference*, Honolulu, Hawaii, April.

Blair, M., Canfield, R.A. and Roberts Jr., R.W. (2005), "Joined-wing aeroelastic design with geometric nonlinearity", *J. Aircraf.*, **42**(4), 832-848.

Cavallaro, R., Demasi, L. and Bertuccelli, F. (2013a), "Risks of linear design of joined wings: a nonlinear dynamic perspective in the presence of follower forces", *Proceedings of the 54th AIAA/ASME/ASCE/ AHS/ASC Structures, Structural Dynamics, and Materials Conference*, April.

Cavallaro, R., Demasi, L., Bertuccelli, F. and Benson, D.J. (2013b), "Risks of linear design of joined wings: a nonlinear dynamic perspective in the presence of follower forces", *CEAS Aeronaut. J.*, 1-20.

Cavallaro, R., Demasi, L. and Passariello, A. (2012), "Nonlinear analysis of PrandtlPlane joined wings - Part II: effects of anisotropy", *Proceedings of the 53rd AIAA/ASME/ASCE/AHS/ASC Structures, Structural Dynamics, and Materials Conference*, Honolulu, Hawaii, April.

Cavallaro, R., Demasi, L. and Passariello, A. (2014a), "Nonlinear analysis of PrandtlPlane joined wings: effects of anisotropy", *AIAA J.*, **52** (5), 964-980.

Cavallaro R., Iannelli, A., Demasi, L. and Razon, A.M. (2014b), "Phenomenology of nonlinear aeroelastic responses of highly deformable joined-wings configurations", *AIAA Science and Technology Forum and Exposition: 55th AIAA/ASME/ASCE/AHS/ASC Structures, Structural Dynamics, and Materials Conference*, National Harbor, Maryland, January.

Cebral, J.R. and Lohner, R. (1997), "Conservative load projection and tracking for fluid-structure problems", *AIAA J.*, **35**(4), 687-692.

Celniker, G. and Gossard, D. (1991), "Deformable curve and surface finite-elements for free-form shape design", *Comput. Graph.*, **25**(4), 257-266.

Chambers, J.R. (2005), *Innovation in Flight: Research of the NASA Langley Research Center on Revolutionary Advanced Concepts for Aeronautics*, NASA.

DalCanto, D., Frediani, A., Ghiringhelli, G.L. and Terraneo, M. (2012), "The lifting system of a PrandtlPlane, Part 1: design and analysis of a light alloy structural solution", *Variational Analysis and Aerospace Engineering: Mathematical Challenges for Aerospace Design*, Springer US, 211-234.

Demasi, L., Cavallaro, R. and Razon, A. (2013a), "Postcritical analysis of PrandtlPlane joined-wing configurations", *AIAA J.*, **51**(1), 161-177.

Demasi, L., Cavallaro, R. and Bertuccelli, F. (2013b), "Post-critical analysis of joined wings: the concept of snap-divergence as a characterization of the instability", *54th AIAA/ASME/ASCE/AHS/ASC Structures, Structural Dynamics, and Materials Conference*, Boston, Massachusetts, April.

Demasi, L., Dipace, A., Monegato, G. and Cavallaro, R. (2014), "Invariant formulation for the minimum induced drag conditions of non-planar wing systems", *AIAA J.*, doi: 10.2514/1.J052837.

Demasi, L. and Livne, E. (2007), "The structural order reduction challenge in the case of geometrically nonlinear joined-wing configurations", *Proceedings of the 48th AIAA/ASME/ASCE/AHS/ASC Structures, Structural Dynamics & Materials Conference*, Honolulu, Hawaii, April.

Demasi, L. and Livne, E. (2009a), "Contributions to joined-wing aeroelasticity", *International Forum on Aeroelasticity and Structural Dynamics Conference*, Seattle, Washington, June.

Demasi, L. and Livne, E. (2009b), "Dynamic aeroelasticity of structurally nonlinear configurations using linear modally reduced aerodynamic generalized forces", *AIAA J.*, **47**, 71-90.

Demasi, L. and Livne, E. (2009c), "Aeroelastic coupling of geometrically nonlinear structures and linear unsteady aerodynamics: Two formulations", *J. Fluid. Struct.*, **25**(5), 918 -935.

Demasi, L. and Palacios, A. (2010), "A reduced order nonlinear aeroelastic analysis of joined wings based on the proper orthogonal decomposition", *Proceedings of the 51st AIAA/ASME/ASCE/AHS/ASC Structures, Structural Dynamics & Materials Conference*, Orlando, Florida, April.

Deparis, S., Discacciati, M., Fourestey, G. and Quarteroni, A. (2006), "Fluid-structure algorithms based on Steklov-Poincaré operators", *Comput. Meth. Appl. Mech. Eng.*, **195**(4143), 5797-5812.

Divoux, N. and Frediani, A. (2012), "The lifting system of a PrandtlPlane, Part 2: preliminary study on flutter characteristics", *Variational Analysis and Aerospace Engineering: Mathematical Challenges for Aerospace Design*, Springer US, 235-267.

Dowell, E., Edwards, J. and Strganac, T. (2003), "Nonlinear aeroelasticity", *J. Aircraf.*, **40**(5), 857-874.

Felippa, C. and Geers, T.L. (1988), "Partitioned analysis for coupled mechanical systems", *Eng. Comput.*, **5**(2), 123-133.

Frediani, A. (1999), "Large Dimension Aircraft", US Patent 5,899,409.

Frediani, A. (2002), "New Large Aircraft", European Patent EP 0716978B1.

Frediani, A. (2003), "Velicolo Biplano ad Ali Contrapposte", Italian Patent FI 2003A000043.

Frediani, A., Cipolla, V. and Rizzo, E. (2012), "The PrandtlPlane configuration: overview on possible applications to civil aviation", *Variational Analysis and Aerospace Engineering: Mathematical Challenges for Aerospace Design*, Springer US, 179-210

Frediani, A. and Montanari, G. (2009), "Best wing system: an exact solution of the Prandtl's problem", *Variational Analysis and Aerospace Engineering*, Springer, New York, 183-211.

Gordnier, R.E. and Melville, R.B. (2001), "Numerical simulation of limit-cycle oscillations of a cropped delta wing using the full navier-stokes equations", *Int. J. Comput. Fluid Dyn.*, **14**(3), 211-224.

Gordnier, R.E. (2003), "Computation of limit-cycle oscillations of a delta wing", *J. Aircraf.*, **40**(6), 1206-1208.

Harder, R.L. and Desmarais, R.N. (1972), "Interpolation using surface splines", *J. Aircraf.*, **9**(2), 189-191.

Lancaster, P. and Salkauskas, K. (1981), "Surfaces generated by moving least squares methods", *Math. Comput.*, **37**(155), 141-158.

Lange, R.H., Cahill, J.F., Bradley, E.S., Eudaily, R.R., Jenness, C.M. and Macwilkinson, D.G. (1974), "Feasibility Study of the Transonic Biplane Concept for Transport Aircraft Applications", NASA.

Liu, G. (2010), *Mesh Free Methods: Moving Beyond the Finite Element Method*, Taylor & Francis.

Lucia, D. (2005), "The SensorCraft configurations: a non-linear AeroServoElastic challenge for aviation", *Proceedings of the 46th AIAA/ASME/ASCE/AHS/ASC Structures, Structural Dynamics and Materials Conference, American Institute of Aeronautics and Astronautics*, Austin, Texas, April.

Katz, J. and Plotkin, A. (2001), *Low-Speed Aerodynamics*, Cambridge Aerospace Series, Cambridge University Press.

Kuhl, D. and Ramm, E. (1999), "Generalized energy momentum method for non-linear adaptive shell dynamics," *Comput. Meth. Appl. Mech. Eng.*, **178**(34), 343-366.

Küttler, U. and Wall, W.A. (2008), "Fixed-point fluid/structure interaction solvers with dynamic relaxation", *Comput. Mech.*, **43**, 61-72.

Miranda, L.R. (1974), "Boxplane Wing and Aircraft", US Patent.

Murua, J., Palacios, R. and Graham, J.M.R. (2012), "Applications of the unsteady vortex-lattice method in aircraft aeroelasticity and flight dynamics", *Prog. Aerosp. Sci.*, **55**(0), 46-72.

Nayroles, B., Touzot, G. and Villon, P. (1992), "Generalizing the finite element method: diffuse

approximation and diffuse elements", *Comput. Mech.*, **10**, 307-318.
Patil, M.J. (2003), "Nonlinear aeroelastic analysis of joined-wing aircraft", *Proceedings of the 44th AIAA/ASME/ASCE/AHS/ ASC Structures, Structural Dynamics & Materials Conference*, Norfolk, Virginia, April.
Prandtl, L. (1924), "Induced Drag of Multiplanes", Technical Report, NACA.
Phlipot, G., Wang, X., Mignolet, M., Demasi, L., and Cavallaro, R. (2014), "Reduced order modeling for the nonlinear geometric response of some joined wings", *Proceedings of the 55th AIAA/ASME/ASCE/AHS/ ASC Structures, Structural Dynamics, and Materials Conference*, National Harbor, Maryland, January.
Quaranta, G., Mantegazza, P. and Masarati, P. (2003), "Assessing the local stability of periodic motions for large multibody nonlinear systems using POD", *J. Sound Vib.*, **271**, 1015-1038.
Quaranta, G., Masarati, P. and Mantegazza, P. (2005), "A conservative mesh-free approach for fluid structure problems in coupled problems", *Proceedings of the International Conference for Coupled Problems in Science and Engineering*, Santorini, Greece, May.
Rodden, W.P., Taylor, P.F. and McIntosh, S.C. (1998), "Further refinement of the subsonic doublet-lattice method", *J. Aircraf.*, **35**(5), 720-727.
Seydel, R. (2009), *Practical Bifurcation and Stability Analysis*, Springer.
Strogatz, S.H. (1994), *Nonlinear Dynamics and Chaos: With Applications to Physics, Biology, Chemistry, And Engineering (Studies in Nonlinearity)*, Perseus Books Group.
Thompson, J. and Stewart, H. (1986), *Nonlinear Dynamics and Chaos: Geometrical Methods for Engineers and Scientists*, Wiley.
Tiso, P., Demasi, L., Teunisse, N. and Cavallaro, R. (2014), "A computational method for structurally nonlinear joined wings based on modal derivatives", *Proceedings of the 55th AIAA/ASME/ASCE/AHS/ ASC Structures, Structural Dynamics, and Materials Conference*, National Harbor, Maryland, January.
Weisshaar, T. and Lee, D.H. (2002), "Aeroelastic tailoring of joined-wing configurations", *Proceedings of the 43rd AIAA/ASME/ASCE/AHS/ASC Structures, Structural Dynamics, and Materials Conference*, Denver, Colorado, 22-25 April.
Wolkovitch, J. (1986), "The joined wing aircraft: an overview", *J. Aircraf.*, **23**(3), 161-178.

EC